

# CosmoReionMC: A package for estimating cosmological and astrophysical parameters using CMB, Lyman- $\alpha$ absorption and global 21 cm data

Atrideb Chatterjee<sup>1\*</sup>, Tirthankar Roy Choudhury<sup>1†</sup> and Sourav Mitra<sup>2</sup>

<sup>1</sup>*National Centre for Radio Astrophysics, TIFR, Post Bag 3, Ganeshkhind, Pune 411007, India*

<sup>2</sup>*Department of Physics, Surendranath College, 24/2 M. G. Road, Kolkata 700009, India*

Accepted XXX. Received YYY; in original form ZZZ

## ABSTRACT

We present a Markov Chain Monte Carlo (MCMC)-based parameter estimation package, CosmoReionMC, to jointly constrain cosmological parameters of the  $\Lambda$ CDM model and the astrophysical parameters related to hydrogen reionization. The package is based on a previously developed physically motivated semi-analytical model for reionization, a similar semi-analytical model for computing the global 21 cm signal during the cosmic dawn and using an appropriately modified version of the publicly available CAMB for computing the CMB anisotropies. These calculations are then coupled to an MCMC ensemble sampler emcee to compute the posterior distributions of the model parameter. The model has twelve free parameters in total: five cosmological and seven related to the stellar populations. We constrain the parameters by matching the theoretical predictions with CMB data from Planck, observations related to the quasar absorption spectra and, for the first time, the global 21 cm signal from EDGES. We find that incorporating the quasar spectra data in the analysis tightens the bounds on the electron scattering optical depth  $\tau$  and consequently the normalization  $A_s$  of the primordial matter power spectrum (or equivalently  $\sigma_8$ ). Furthermore, when we include the EDGES data in the analysis, we find that an early population of metal-free stars with efficient radio emission is necessary to match the absorption amplitude. The CosmoReionMC package should have interesting future applications, e.g., probing non-standard extensions to the  $\Lambda$ CDM model.

**Key words:** intergalactic medium – dark ages, reionization, first stars – stars: Population III – cosmology: theory.

## 1 INTRODUCTION

Our Universe has gone through two-phase transitions between the ionized and neutral states of the hydrogen atom, one at  $z \approx 1100$ , when the free electrons from ionized plasma recombine with the protons to form atomic hydrogen and another at  $z \approx 6$  when the neutral Universe becomes almost completely ionized. The later epoch ( $z \approx 6 - 20$ ), when the first stars form and the photons coming from them, start to heat up and ionize the intergalactic medium (IGM), is broadly known as Epoch of Reionization (EoR) (Barkana & Loeb 2001; Loeb & Barkana 2001; Choudhury 2009; Dayal & Ferrara 2018). The very early phase of reionization when the first stars just started to form, is sometimes referred to as the Cosmic Dawn (CD). The Cosmic Microwave Background (CMB) photons coming from the last scattering surface of the Universe (at  $z \approx 1100$ ) interact with the free electrons in the IGM produced during the EoR. As a result of this interaction, the CMB temperature anisotropy gets suppressed whereas the amplitude of the EE polarization of the CMB anisotropy angular power spectrum gets enhanced (Sunyaev & Zeldovich 1980; Vishniac 1987; Hu 2000; Hu & Dodelson 2002; McQuinn et al. 2005). It is well known that using the observed CMB anisotropies and assuming a reionization history, the direction-averaged Thomson scattering optical depth,  $\tau$ , can be computed. It has been a common

practice to compare the value of the optical depth estimated from the reionization model with that of the CMB angular power spectrum  $C_l$  observations to constrain the free parameters of the model (Planck Collaboration et al. 2016, 2020; Hu & Holder 2003; Mitra et al. 2012; Mortonson & Hu 2008; Pandolfi et al. 2011; Mitra et al. 2015, 2018a).

While calculating  $\tau$  from the observed CMB angular power spectra, one usually assumes a redshift-symmetric tanh model of reionization (Lewis 2008; Planck Collaboration et al. 2016, 2020) or a model described by polynomials (Hazra & Smoot 2017). However, the value of optical depth, in principle, depends on the details of the reionization history used, and hence the optical depths calculated from the tanh or polynomial models should not be compared with that estimated from the model which assumes a different reionization history. One way to overcome the problem is to connect a reionization model with a “CMB anisotropy code” e.g. Code for Anisotropies in the Microwave Background (CAMB) (Lewis 2013) or the Cosmic Linear Anisotropy Solving System (CLASS) (Lesgourgues 2011) and then compare with the observed CMB power spectrum to constrain the free parameters of the reionization model (Pandolfi et al. 2011; Mitra et al. 2012). Such analysis with a physically motivated reionization model had been carried out in the past (Miranda et al. 2017; Qin et al. 2020). However, in Miranda et al. (2017), the authors varied only the model parameters and  $\tau$  but not any other cosmological parameters, whereas other studies (Miranda et al. 2017; Planck Collaboration et al. 2020; Douspis et al. 2015; Mitra et al. 2015) sug-

\* E-mail: atrideb@ncra.tifr.res.in

† E-mail: tirth@ncra.tifr.res.in

gest that parameters related to reionization have degeneracies with the cosmological parameters and therefore could possibly introduce bias in the obtained constraints on the reionization model parameters. Hence the right approach to handle this problem would be to constrain the cosmological and the reionization parameters simultaneously (Mitra et al. 2012; Qin et al. 2020; Hazra et al. 2020) by comparing with CMB and astrophysical data sets.

Recently a sky-averaged global 21 cm signal spanning the redshift range  $z \approx 13 - 22$  has been claimed to be detected by Experiment to Detect the Global EoR Signal (EDGES) collaboration (Bowman et al. 2018). Although the “true” origin of the signal is still in debate (Hills et al. 2018; Bradley et al. 2019; Singh & Subrahmanyam 2019; Sims & Pober 2020), it is indeed a promising probe to find out the epoch of structure formation (for review look at Furlanetto et al. 2006) as this signal captures the information about first stars during the cosmic dawn (Chatterjee et al. 2020; Mebane et al. 2020; Schauer et al. 2019). However, modelling of the 21 cm signal at the cosmic dawn depends on the cosmological parameters. For example, any parameter which affects the formation of dark matter haloes (say, the amplitude of the primordial matter power spectrum) will also affect the timing of the formation of first stars and shift the absorption trough of this signal to a different redshift. Thus, adding global 21 cm observation along with the reionization and CMB observations should potentially provide an independent way to put new constraints on the cosmological parameters. In fact, previous studies (Liu et al. 2016) had predicted that the degeneracy between  $\tau$  and  $A_s$  can be alleviated by using the Global 21 cm signal. But of course at that time the global 21 cm signal had not been detected so they could not apply their method on the actual observation.

A huge body of works in recent years (Greig & Mesinger 2015; Mesinger et al. 2016; Greig & Mesinger 2017a,b; Hassan et al. 2017; Kern et al. 2017; Greig & Mesinger 2018; Schmit & Pritchard 2018; Park et al. 2019; Gillet et al. 2019; Ghara et al. 2021) have been devoted in building different kinds of parameter estimation techniques which use 21 cm signal (both global and power spectrum) and reionization related observations to put constraints on the model parameters. However, they varied only the model parameters and kept the cosmological parameters fixed to their best fit values, except Kern et al. (2017) varied both the model parameters and the cosmological parameters. In Kern et al. (2017), the authors also varied the cosmological parameters along with the model parameters and they use an emulator based MCMC approach to constrain these parameters using 21 cm power spectrum as their observation.

In this work, we develop a parameter estimation routine, called CosmoReionMC, which combines a semi-analytical physically motivated reionization and cosmic dawn model with the publicly available Boltzmann solver code CAMB and perform a Markov Chain Monte Carlo (MCMC) analysis to put constraints on the cosmological and model parameters simultaneously using the CMB, reionization and global 21 cm (EDGES) observation. The aim of this work is two-fold: First, we investigate in detail the impact of choosing a physically motivated reionization scenario over the tanh model on the constraints on the  $\Lambda$ CDM cosmological parameters with the most recent CMB data, thus updating the results obtained by Mitra et al. (2015, 2018a). Secondly, for the first time, we explore the effect of combining the global 21 cm experiments with the reionization and CMB observations (with full likelihoods of the CMB data) on the parameter estimation.

The paper is organized as follows. In Section 2, we describe the theoretical model used to compute the reionization and 21 cm signal. Section 3 describes the joint constraints on cosmological and reionization parameters after adding reionization observations with CMB

observations. The effect of including the 21 cm observation along with the reionization and CMB observation is discussed in detail in Section 4. We summarize our results and conclusion in Section 5.

## 2 THE THEORETICAL MODEL

The theoretical model used in this work contains several components which have been combined efficiently to compute the observable. We discuss the model components one by one.

### 2.1 Reionization Model

We use a reionization model proposed by Choudhury & Ferrara (2005), Choudhury & Ferrara (2006) (referred as CF model hereafter) and later slightly modified in Mitra et al. (2011). Here we summarize the main features of the reionization model used in this analysis.

(i) The model computes the evolution of the ionization and thermal state of the neutral, HII and HeIII regions of the IGM separately, simultaneously and self-consistently.

(ii) The inhomogeneities of the intergalactic medium (IGM) is described using the method outlined in Miralda-Escudé (2003). The probability distribution of the over-densities are assumed to follow a log-normal distribution in the low density region, whereas the high density region of the IGM is described using a power law distribution. In this model, the reionization is assumed to be complete once all the low density regions are ionized, i.e., the volume filling factor  $Q_{\text{HII}}$  of ionized hydrogen in low density regions becomes unity.

(iii) The sources of reionization in this model are assumed to be quasars, PopII and PopIII stars. For the stellar sources, the photon production rate is assumed to be of the form

$$\begin{aligned} \dot{n}_\nu(z) &= \dot{n}_\nu^{\text{II}} + \dot{n}_\nu^{\text{III}} \\ &= \rho_b \left[ f_*^{\text{II}} f_{\text{esc}}^{\text{II}} \left( \frac{dN_\nu}{dM} \right)_{\text{II}} \frac{df_{\text{coll,II}}}{dt} + f_*^{\text{III}} f_{\text{esc}}^{\text{III}} \left( \frac{dN_\nu}{dM} \right)_{\text{III}} \frac{df_{\text{coll,III}}}{dt} \right], \end{aligned} \quad (1)$$

where  $\rho_b$  is the mean comoving density of baryons in the IGM,  $f_*$  is the star formation efficiency,  $f_{\text{esc}}$  is the escape fraction of the ionizing photons entering IGM and  $dN_\nu/dM$  is the number of photons emitted per frequency range per unit mass of stars. The total number of hydrogen ionizing photons from stellar sources is then

$$\begin{aligned} \dot{n}_{\text{ph}}(z) &= \int_{\nu_H}^{\infty} d\nu \dot{n}_\nu(z) \\ &= n_b \left[ N_{\text{ion,II}} \left( \frac{df_{\text{coll,II}}}{dt} \right) + N_{\text{ion,III}} \left( \frac{df_{\text{coll,III}}}{dt} \right) \right], \end{aligned} \quad (2)$$

where  $\nu_H$  is the threshold frequency for hydrogen photoionization,  $n_b$  is the mean comoving number density of baryons in the IGM and

$$N_{\text{ion}} \equiv m_p \int_{\nu_H}^{\infty} f_* f_{\text{esc}} \left( \frac{dN_\nu}{dM} \right) d\nu \quad (3)$$

is the number of ionizing photons escaping into the IGM per baryons in stars, with  $m_p$  being the proton mass. In this work, we assume the parameters  $f_*$ ,  $f_{\text{esc}}$  for each stellar population to be independent of the halo mass  $M$  and redshift  $z$  which allows us to keep the number of free parameters under control. These assumptions are clearly simplified as there are indications that these have non-trivial dependencies on  $M$  and  $z$ , however, there is still no consensus on the actual form for this dependence (see, e.g., Yajima et al. 2012; Mitra et al. 2013; Wise et al. 2014; Paardekooper et al. 2015; Kimm et al.

2017, 2019; Qin et al. 2017; Davies et al. 2019; Greig et al. 2020; Park et al. 2020).

The fraction of mass in collapsed haloes forming PopII and PopIII stars at redshift  $z$  are given by

$$f_{\text{coll,II}} = \frac{1}{\rho_m} \int_{M_{\text{min}}(z)}^{\infty} dM [1 - f_{\text{III}}(M, z)] M \frac{\partial n(M, z)}{\partial M}, \quad (4)$$

and

$$f_{\text{coll,III}} = \frac{1}{\rho_m} \int_{M_{\text{min}}(z)}^{\infty} dM f_{\text{III}}(M, z) M \frac{\partial n(M, z)}{\partial M}, \quad (5)$$

where  $\rho_m$  is the mean comoving density of dark matter and  $\partial n / \partial M$  is number density of haloes per unit comoving volume per unit mass range, computed using the Sheth-Tormen form (Sheth & Tormen 1999; Sheth et al. 2001). The quantity  $f_{\text{III}}(M, z)$  is the fraction of haloes of mass  $M$  that are forming PopIII stars at  $z$ .

A crucial ingredient of the model is to compute the transition from metal-free PopIII to the usual PopII stars, which essentially determines the form of  $f_{\text{III}}(M, z)$ . The transition is regulated by chemical feedback from the PopIII stars and hence depends on the merger history of dark matter haloes and mixing of metals in the IGM (Jaacks et al. 2018; Sarmiento et al. 2019; Maio et al. 2010, 2011). In reality, the transition is likely to be complex with different regions of the universe being metal-contaminated at different times. Modelling the effect in a self-consistent manner is beyond the scope of any semi-analytical model like ours. We thus assume that the PopIII  $\rightarrow$  PopII transition occurs at a redshift  $z_{\text{trans}}$  with a width  $\delta z$ , the exact form being given by

$$f_{\text{III}}(M, z) = f_{\text{III}}(z) = \frac{1}{2} \left[ 1 + \tanh \left( \frac{z - z_{\text{trans}}}{\delta z} \right) \right]. \quad (6)$$

The transition redshift  $z_{\text{trans}}$  is a free parameter of the model while the width  $\delta z$  is taken to be that corresponding to the dynamical time-scale of collapsed objects at  $z_{\text{trans}}$ . The reason for choosing so is because the star formation in haloes is expected to be spread over the dynamical time (Chiu & Ostriker 2000), hence the same time-scale will determine the decline of the PopIII stars. Furthermore, we find that typically  $\delta z \sim 2$  at  $z_{\text{trans}} \sim 16$  which is consistent with the parametric PopIII star formation rate found by Chatterjee et al. (2020) to match the EDGES data.

As discussed in Choudhury & Ferrara (2005), the quantity  $dN_{\nu}/dM$  depends on the stellar spectra and IMF of the stars. For PopII stars, this number has been calculated from the stellar population synthesis models of Bruzual & Charlot (2003) using a standard Salpeter IMF in the mass range  $1 - 100 M_{\odot}$  with a metallicity of  $0.05 M_{\odot}$ . For PopIII stars, it is calculated using stellar spectra of very high mass stars ( $> 300 M_{\odot}$ ) (Schaerer 2002).

We further fix the PopII star formation efficiency  $f_{*}^{\text{II}}$  by matching our predictions with the observed UV luminosity function ( $6 \leq z \leq 10$ ) (Bouwens et al. 2006, 2015; Oesch et al. 2018, 2014; Livermore et al. 2017; Ishigaki et al. 2018). Obviously, we implicitly assume here that the observed stars at these redshifts are dominantly PopII. This is justified because, as we will see later, the data implies the PopIII stars to decline by  $z \sim 15$ . We found that to match with the observed UV luminosity function, we require  $f_{*}^{\text{II}} \sim 0.01$ , and hence we fix this value throughout the paper.<sup>1</sup>

For the quasars, the rate of ionizing photons per unit volume per unit frequency range has been computed following the procedure outlined in Choudhury & Ferrara (2005), i.e., from the relation

$$\dot{n}_{\nu, Q}(z) = \int_0^{\infty} dL_B L_B \psi(L_B, z) \frac{L_{\nu}(L_B)}{h_p \nu}, \quad (7)$$

where  $\psi$  is the quasar luminosity function taken from the recent compilation of Kulkarni et al. (2019b),  $L_B$  is the B-band luminosity and  $h_p$  is the Planck's constant. Assuming the luminosity ( $L_{\nu}$ ) of all quasars to follow a power law with  $L_{\nu} \propto \nu^{-\alpha}$  with  $\alpha = 1.57$  for  $\lambda \sim 500$  to  $\sim 1200 \text{ \AA}$  (Schirber & Bullock 2003; Telfer et al. 2002), we can write

$$\frac{L_{\nu}(L_B)}{\text{erg s}^{-1} \text{ Hz}^{-1}} = \frac{L_B}{L_{\odot, B}} 10^{18.05} \left( \frac{\nu}{\nu_H} \right)^{-1.57}, \quad (8)$$

where  $\nu_H$  is the threshold frequency for photoionization of hydrogen. Putting equation (8) in equation (7) one can calculate the ionizing photon production rate from quasars. The only role the quasars play in our model is to reionize HeII at  $z \sim 3.5$ . Since most of the work in this paper is concentrated on the ionization of hydrogen, the details of the ionizing photons from quasars can be ignored for the rest of the paper.

(iv) The value of the collapsed fraction  $f_{\text{coll}}$  depends on the minimum mass  $M_{\text{min}}(z)$  of haloes that are capable of forming stars and producing ionizing photons. In the neutral regions, we consider only atomically cooled haloes while calculating the minimum mass.<sup>2</sup> In addition, the radiative feedback from stars has also been implemented to account for the fact that once the first stars form they will ionize and heat the surrounding IGM. This implies that the minimum halo mass for star formation is higher in the ionized regions (Ocvirk et al. 2016, 2019; Katz et al. 2019; Wu et al. 2019; Hutter et al. 2020) and thus star formation is suppressed in low mass haloes through a Jeans mass prescription (Choudhury & Ferrara 2005). As our model tracks the thermal history of the ionized region separately from the neutral region of the IGM, this effect has easily been implemented while computing the minimum halo mass of the star forming region.

(v) Assuming that only the high density regions of the IGM determine the mean free path of the photons (as discussed in Miralda-Escudé 2003), the CF reionization model computes it as

$$\lambda_{\text{mfp}} = \frac{\lambda_0}{[1 - F_V(\Delta_i)]^{2/3}} \quad (9)$$

where  $\lambda_0$  is a free parameter of the model and  $F_V$  is the volume fraction of the ionized region, i.e., regions with overdensities less than  $\Delta_i$  (the high-density regions are assumed to be self-shielded in the CF reionization model). The mean free path can be used to calculate the redshift distribution  $dN_{\text{LL}}/dz$  of the Lyman-limit systems, which can then be compared with the corresponding observations (Ribaud et al. 2011; O'Meara et al. 2013; Fumagalli et al. 2013; Prochaska et al. 2010; Crighton et al. 2019) to obtain constraints on  $\lambda_0$ .

(vi) The hydrogen photoionization rate ( $\Gamma_{\text{PI}}$ ) can be obtained from the photon production rate  $\dot{n}_{\text{ph}}(z)$  and the mean free path  $\lambda_{\text{mfp}}$  using

$$\Gamma_{\text{PI}}(z) = (1 + z)^3 \int_{\nu_H}^{\infty} d\nu \lambda_{\text{mfp}}(\nu, z) \dot{n}_{\text{ph}}(z) \sigma_H(\nu), \quad (10)$$

<sup>2</sup> There are studies which indicate that the first stars would have formed in minihaloes that are cooled via  $\text{H}_2$  molecules (Haiman et al. 1997; Bromm & Loeb 2003; Valiante et al. 2016). The efficiency of these haloes will depend on the severity of the dissociating Lyman-Werner (LW) feedback (Omukai & Palla 2001; Shang et al. 2010; Wolcott-Green et al. 2011; Fialkov et al. 2013; Visbal et al. 2014). The presence of molecular cooling and LW feedback have been ignored in this work.

<sup>1</sup> The values of  $f_{*}^{\text{II}}$  in this work are lower than those obtained by Mitra et al. (2015). The main reason for this is that Mitra et al. (2015) used the halo mass function of Press & Schechter (1974), while we are using the one given by (Sheth & Tormen 1999; Sheth et al. 2001). In addition, the UV luminosity function data have been updated to include all the latest observations.

where  $\sigma_H(\nu)$  is the hydrogen photoionization cross-section. Similar equations can be used for calculating the photoionization rate for HeII as well.

The CF reionization has been applied in several different kinds of studies, e.g., constraining escape fraction of ionizing photons from galaxies (Mitra et al. 2013), quantifying the contribution of quasars to hydrogen reionization by including helium reionization data in the analysis (Mitra et al. 2018a), constraining reionization in tilted flat and untilted non-flat dynamical dark energy inflation models (Mitra et al. 2018b, 2019), constraining the primordial magnetic fields (Pandey et al. 2015).

## 2.2 The global 21 cm signal from cosmic dawn

The 21 cm global brightness temperature is calculated following the calculations of Furlanetto (2006); Chatterjee et al. (2019). The sky averaged 21 cm brightness temperature can be calculated using (Chatterjee et al. 2019)

$$\delta T_b(\nu) \approx 10.1 \text{ mK } x_{\text{HI}}(z) \left[ 1 - \frac{T_\gamma(z)}{T_S(z)} \right] (1+z)^{1/2}, \quad (11)$$

where  $T_\gamma$  is the background radiation temperature,  $T_S$  is the neutral hydrogen spin temperature and  $x_{\text{HI}}$  is the neutral hydrogen fraction in the IGM. The spin temperature  $T_S$  is computed using (Field 1958)

$$T_S^{-1} = \frac{T_\gamma^{-1} + x_c T_K^{-1} + x_\alpha T_\alpha^{-1}}{1 + x_c + x_\alpha}, \quad (12)$$

where  $T_K$  is the kinetic temperature of the IGM,  $T_\alpha$  is the Ly $\alpha$  color temperature and  $x_c$  and  $x_\alpha$  are respectively the collisional and Ly $\alpha$  coupling coefficients. As the optical depth of the Ly $\alpha$  is very high in the epoch of cosmic dawn,  $T_\alpha$  rapidly approaches  $T_K$ . Moreover, in the redshift range observed using EDGES where the 21 cm signal calculations are most relevant, the collisions turn out to be negligible  $x_c \ll 1$  (Furlanetto 2006). With these approximation, equation (12) simplifies to

$$T_S^{-1} = \frac{T_\gamma^{-1} + x_\alpha T_K^{-1}}{1 + x_\alpha}. \quad (13)$$

In the CF reionization model, the gas kinetic temperature is determined mainly by two processes, namely, the adiabatic cooling and the photoheating from UV photons. During the cosmic dawn, however, the heating is dominated by X-rays arising from star formation. To account for this fact, we include the X-ray heating term in the temperature evolution equation. Since the X-ray heating tends to become sub-dominant compared to the UV heating once the reionization starts, we switch off the X-ray heating in the reionization epoch. This allows us to keep the code numerically efficient.

To model the X-ray heating, we assume that the X-ray emissivity is proportional to the star formation rate. This is motivated by the observational result that the star formation rate and the X-ray luminosity of galaxies observed in the local Universe are strongly correlated (Mineo et al. 2012). We assume that such a correlation holds at high- $z$  and write the X-ray energy injection rate per unit comoving volume as

$$\frac{\epsilon_X}{\text{J s}^{-1} \text{Mpc}^{-3}} = 3.4 \times 10^{33} \frac{\rho_b \left[ f_{\text{II}}^{\text{II}} f_{Xh}^{\text{II}} \frac{df_{\text{coll,II}}}{dt} + f_{\text{III}}^{\text{III}} f_{Xh}^{\text{III}} \frac{df_{\text{coll,III}}}{dt} \right]}{M_\odot \text{Mpc}^{-3} \text{yr}^{-1}}, \quad (14)$$

where  $f_{Xh} = f_X f_h$  (for both PopII and PopIII stars). The unknown

normalization factor  $f_X$  takes into account any difference between local observations and high redshift, and  $f_h$  is the heating fraction of the total X-ray photons in the IGM (the other part helps in ionization).

The Ly $\alpha$  coupling coefficient  $x_\alpha$  is determined by the background Ly $\alpha$  flux  $J_\alpha$  through the relation

$$x_\alpha = \frac{1.81 \times 10^{11}}{(1+z)} S_\alpha \frac{J_\alpha}{\text{cm}^{-2} \text{s}^{-1} \text{Hz}^{-1} \text{sr}^{-1}}, \quad (15)$$

where  $S_\alpha$  is a factor of order unity. It accounts for the detailed atomic physics involved in the scattering process. For simplicity, we fix  $S_\alpha = 1$ . The flux can be calculated from the photon production rate as

$$J_\alpha(z) = \frac{c}{4\pi} (1+z)^3 \int_z^{z_{\text{max}}} dz' \left[ f_\alpha^{\text{II}} \dot{n}_{\nu'}^{\text{II}}(z') + f_\alpha^{\text{III}} \dot{n}_{\nu'}^{\text{III}}(z') \right] \left| \frac{dt'}{dz'} \right|, \quad (16)$$

where  $f_\alpha$  (defined for both the stellar populations) is a normalization parameter that takes into account any uncertainties in the Ly $\alpha$  flux that may arise from the unknown properties of the high redshift galaxies. For example, it is possible that some fraction of Ly $\alpha$  photons may not escape into IGM because of some unknown interaction within the ISM, in that case the uncertainty will get absorbed in this parameter. The upper limit  $z_{\text{max}}$  of the integral accounts for the fact that continuum ionizing would be absorbed in the IGM and not contribute the Ly $\alpha$  radiation. The limit is calculated using (Chatterjee et al. 2020)

$$1 + z_{\text{max}} = \frac{\nu_H}{\nu_\alpha} (1+z), \quad (17)$$

where  $\nu_\alpha$  is the Ly $\alpha$  frequency.<sup>3</sup> Note that the photon production rate  $\dot{n}_\nu$  is proportional to  $f_*$ , see equation (1), hence  $J_\alpha$  is proportional to the combination  $f_* f_\alpha$  of the two populations.

It is well-known that the amplitude of the EDGES absorption signal (Bowman et al. 2018) cannot be explained by standard models of galaxy formation. There have been discussions that the cosmological signal implied by EDGES may be an artefact of different systematics (Hills et al. 2018; Bradley et al. 2019; Singh & Subrahmanyam 2019; Sims & Pober 2020). While the confirmation of the result will require more tests with different instruments, we, for the time being, assume that the cosmological 21 cm signal is indeed that implied by Bowman et al. (2018). Various speculations have been made in order to explain the excess dip of the EDGES signal, e.g., some exotic dark matter models where the dark matter particles interact with the baryons (Barkana et al. 2018; Fraser et al. 2018; Pospelov et al. 2018; Slatyer & Wu 2018) and an excess radio background driven by formation of early stars (Feng & Holder 2018; Ewall-Wice et al. 2018; Mirocha & Furlanetto 2019; Fialkov & Barkana 2019; Mebane et al. 2020; Ewall-Wice et al. 2020). We avoid exploring any non-standard dark matter scenarios in this work and consider the latter scenario of excess radio flux. Note that this assumption may have some observational support from the excess observed by the ARCADE-2 experiment (Fixsen et al. 2011), although the origin of the excess is somewhat debatable Seiffert et al. 2011. The radio

<sup>3</sup> The Ly $\alpha$  radiation also leads to heating of the IGM (see, e.g., Ghara & Mellema 2020; Mittal & Kulkarni 2021) which is not incorporated in our model. Since both the Ly $\alpha$  flux and the heating are driven by the collapse rate  $df_{\text{coll}}/dt$ , inclusion of this process should affect the constraints on the efficiency parameters related to the stars. However, we do not expect the constraints on the cosmological parameters to be affected in any significant manner.



background is modelled based on the work of Chatterjee et al. (2019) and calculated using

$$\frac{\epsilon_R}{\text{J s}^{-1} \text{Mpc}^{-3}} = 10^{22} \frac{\rho_b \left[ f_R^{\text{II}} f_R^{\text{II}} \frac{df_{\text{coll,II}}}{dt} + f_R^{\text{III}} f_R^{\text{III}} \frac{df_{\text{coll,III}}}{dt} \right]}{M_\odot \text{Mpc}^{-3} \text{yr}^{-1}}, \quad (18)$$

where,  $f_R$  takes into account the uncertainty one needs to introduce in order to extrapolate the radio-SFR relation from local to high redshift Universe.

It is worth noting that there is still no self-consistent model of producing a strong radio background at high redshifts. There have been concerns whether the accelerating relativistic electrons that produce the excess background can be sustained as their cooling time is much shorter than the Hubble time at  $z \sim 17$  (Sharma 2018). On the other hand, Ewall-Wice et al. (2020) have pointed out that the continuous injection of particles leads to a different time-evolution of the radiation spectrum and hence the concerns may not be that severe.

### 2.3 The CMB anisotropies

Given the reionization model, we need to compute the CMB angular anisotropies, in particular, the angular power spectra  $C_l$  for the temperature and E-mode polarization fluctuations. For this purpose, we use the publicly available python-wrapped CAMB Lewis (2013)<sup>4</sup>, which is an efficient code for computing the CMB anisotropies. The default reionization history used in the CAMB input is the simple tanh parametrization Lewis (2008), which is not sufficient for our work. As was done by Mitra et al. (2012), we modify CAMB to incorporate the reionization history implied by our reionization model. The resulting output can be compared with the CMB data sets in a straightforward manner.

### 2.4 The CosmoReionMC Package

Finally, we combine the various components of the model described in the preceding subsections and combine with a module for carrying out the likelihood analysis. This allows us to do parameter estimation in an efficient manner. The resulting package is named as CosmoReionMC. As discussed later, this package has many potential applications, e.g., put constraints on non standard cosmology, constraining the mass of dark matter particles, non standard dark energy, non-flat cosmological models and many more. We plan to make this package public in the near future.

The likelihood analysis to constrain the parameters is based on MCMC. For this purpose, we develop a module which is inspired from the publicly available CosmoHammer (Akeret et al. 2013) for estimating cosmological parameters. The MCMC routine is driven by the publicly available emcee code (Foreman-Mackey et al. 2013).

In order to connect with the latest python-wrapped CAMB and emcee, the reionization and 21 cm codes have now been written completely in python.<sup>5</sup> We have ensured that the code is optimized in terms of computing efficiency. For example, a typical MCMC run takes about 24 hours using 24 cores.

So to summarize, our parameter estimation package

CosmoReionMC is an efficient combination of (i) a semi-analytical reionization and cosmic dawn model (Choudhury & Ferrara 2005; Chatterjee et al. 2019), (ii) CMB anisotropy code CAMB (Lewis 2013) modified to account for arbitrary reionization histories and (iii) the emcee code (Foreman-Mackey et al. 2013) for the statistical MCMC analysis.

## 3 PARAMETER CONSTRAINTS

We now present the results on the parameter constraints obtained using CosmoReionMC.

### 3.1 Constraints using only CMB data

We first apply our code to obtain constraints on the cosmological parameters using only CMB data. For this purpose, we compare the CMB angular power spectrum predicted by our model with the Planck 2018 observations. The free parameters for this analysis (referred to as **only-CMB** hereafter) are

$$\Theta = \{H_0, \Omega_b h^2, \Omega_c h^2, A_s, n_s, f_{\text{esc}}^{\text{II}}, \lambda_0\}, \quad (19)$$

where the first five parameters are the usual cosmological parameters in the flat  $\Lambda$ CDM model and the last two are the free parameters of our reionization model. We ignore the contribution of PopIII stars in this part of the analysis as it has been shown (Qin et al. 2020; Mitra et al. 2015, 2011) that they are not required for matching the reionization-related observations. To confirm this, we have also run a model including PopIII stars and found that the constraints are consistent with no contribution from PopIII stars. We also found that the constraints on the other parameters are not affected even if we ignore the PopIII contribution.

The main input to the MCMC analysis is the negative of the log-likelihood denoted as  $\mathcal{L}$  (so that the likelihood is  $L \propto \exp(-\mathcal{L})$ ). For the **only-CMB** analysis, this is given by

$$\mathcal{L} = \mathcal{L}_{\text{Pl}}, \quad (20)$$

where  $\mathcal{L}_{\text{Pl}}$  is the log-likelihood function corresponding to the Planck 2018 observations. For  $l \geq 30$ , the joint likelihood for TT, TE and EE fluctuations are computed using the “Plik lite” method where the foreground and other nuisance parameters are marginalized over appropriate prior ranges. For small- $l$  values, we use the likelihoods obtained by the “Commander” approach for TT (Planck Collaboration et al. 2014) and by the “SimAll” algorithm for EE and BB.<sup>6</sup>

The other input to the MCMC analysis is the prior on the free parameters. We assume a broad flat prior for all the seven free parameters, the values are mentioned in “Prior” column of Table 1. For exploring the parameter space with MCMC chains, we use 32 walkers taking  $10^6$  steps. The first 30% steps are removed from the analysis as “burn-in” and the posterior distributions are computed

<sup>6</sup> The details of these likelihoods can be found on the wiki page [https://wiki.cosmos.esa.int/planck-legacy-archive/index.php/CMB\\_spectrum\\_%26\\_Likelihood\\_Code](https://wiki.cosmos.esa.int/planck-legacy-archive/index.php/CMB_spectrum_%26_Likelihood_Code). In particular, we use

hi\_l/plik\_lite/plik\_lite\_v22\_TTEEE.clik for the high- $l$  likelihood,  
low\_l/commander/commander\_dx12\_v3\_2\_29.clik for the low- $l$  TT,  
low\_l/simall/simall\_100x143\_offlike5\_EE\_Aplanck\_B.clik for the low- $l$  EE and  
low\_l/simall/simall\_100x143\_offlike5\_BB\_Aplanck\_B.clik for the low- $l$  BB fluctuations.

<sup>4</sup> <https://camb.readthedocs.io/en/latest/>

<sup>5</sup> As is well known, MCMC analysis requires executing the core code millions of times, hence it needs to be optimized in time. Here, we use Numba (<http://numba.pydata.org>) to make the code much faster so that the execution time becomes somewhat comparable to that of Fortran.

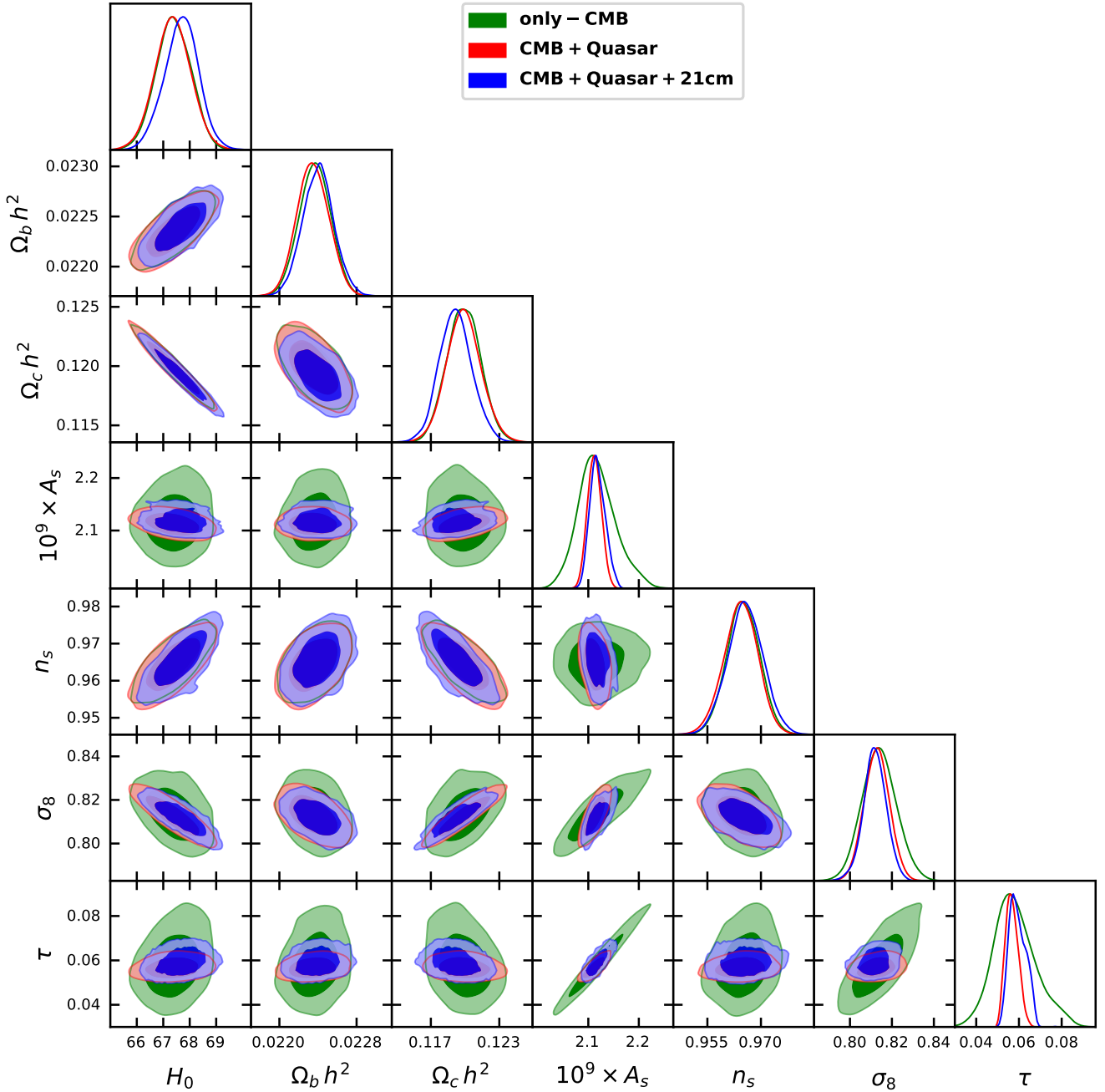


**Figure 1.** The marginalized posterior distributions of cosmological parameters obtained from **only-CMB** (green), **CMB+Quasar** (red) and **CMB+Quasar+21cm** (blue) analyses. We show the 68% and 95% confidence contours in the two-dimensional plots. Note that  $\sigma_8$  and  $\tau$  are derived parameters while the others are free parameters in our model. By comparing the **only-CMB** and **CMB+Quasar** results, it is clear that the inclusion of the quasar absorption data in the analysis leads to much tighter constraints on  $\tau$  and consequently on  $A_s$  and  $\sigma_8$ .

based on the remaining 70% steps. An auto-correlation analysis has been carried out for ensuring the convergence of the chains. We have calculated the integrated autocorrelation time  $\tau_f$  for each parameter-chain (different steps of walkers corresponding to a particular free parameter). We use `autocorr.integrated_time` function of the `emcee` package for this purpose. A parameter-chain is said to be converged if the length of the chain is more than  $100 \times \tau_f$  following a conservative approach discussed in [Foreman-Mackey et al. \(2013\)](#).

The posterior distributions of the model parameters are shown in Figure 1 (green contours). The constraints on the parameters, i.e., the best-fit values along with the mean and 95% C.L are shown in Table 1. We also show the log-likelihood for the best-fit model in the same table. Among the various correlations between the cosmological parameters, one which will play an important role in the subsequent discussions is that between  $A_s$  and  $\tau$  (or equivalently between  $\sigma_8$  and  $\tau$ ). The reason for this tight correlation arises because

Parameter	Prior	only-CMB		CMB+Quasar		CMB+Quasar+21cm	
		best-fit	mean [95% C.L.]	best-fit	mean [95% C.L.]	best-fit	mean [95% C.L.]
$H_0$	[65, 80]	67.21	67.39 [66.10, 68.65]	67.24	67.36 [66.04, 68.70]	67.51	67.68 [66.37, 68.94]
$\Omega_b h^2$	[0.005, 0.05]	0.02234	0.02237 [0.02205, 0.02268]	0.02234	0.02234 [0.02203, 0.02267]	0.02236	0.02240 [0.02208, 0.02272]
$\Omega_c h^2$	[0.01, 0.2]	0.1202	0.1198 [0.1170, 0.1228]	0.1201	0.1198 [0.1169, 0.1229]	0.1198	0.1191 [0.1164, 0.1221]
$10^9 A_s$	[1.0, 3.0]	2.092	2.117 [2.048, 2.200]	2.102	2.112 [2.085, 2.139]	2.105	2.118 [2.091, 2.151]
$n_s$	[0.8, 1.2]	0.9627	0.9650 [0.9559, 0.9739]	0.9625	0.9643 [0.9547, 0.9734]	0.9640	0.9656 [0.9557, 0.9754]
$f_{\text{esc}}^{\text{II}}$	[0.0, 1.0]	0.1372	0.1568 [0.1168, 0.3662]	0.1681	0.1951 [0.1498, 0.2471]	0.1723	0.2096 [0.1514, 0.2850]
$\lambda_0$	[1.0, 10.0]	1.53	3.96 [1.0, 9.99]	4.38	3.97 [2.58, 5.47]	3.97	3.63 [2.06, 5.20]
$f_{Xh}^{\text{II}}$	[0.0, 100.0]	–	–	–	–	4.56	4.30 [1.93, 7.28]
$f_{*,\text{esc}}^{\text{III}}$	[0.0, 1.0]	–	–	–	–	0.0024	0.0030 [0.0008, 0.0055]
$f_{*,\alpha}^{\text{III}}$	[0.0, 50.0]	–	–	–	–	0.534	0.700 [0.157, 2.91]
$f_{*,R}^{\text{III}}$	[ $10^3$ , $10^7$ ]	–	–	–	–	55319.2	53519.8 [24619.8, 89774.5]
$z_{\text{trans}}$	[9.0, 25.0]	–	–	–	–	16.35	16.27 [15.89, 16.68]
$\sigma_8$	–	0.809	0.814 [0.798, 0.830]	0.811	0.812 [0.801, 0.824]	0.812	0.812 [0.802, 0.823]
$\tau$	–	0.0512	0.0581 [0.0402, 0.0802]	0.0533	0.0557 [0.0512, 0.0624]	0.0591	0.0618 [0.0529, 0.0670]
$\mathcal{L}_{\text{pl}}$		693.50		701.50		702.40	
$\mathcal{L}_{\text{Re}}$		–		3.05		3.67	
$\mathcal{L}_{21}$		–		–		201.91	

**Table 1.** Constraints on the model parameters for the three different analyses of the paper. For each parameter, we show the prior along with the best-fit, mean and 95% confidence limits. The parameters  $\sigma_8$  and  $\tau$  are derived. The last three rows show the best-fit log-likelihood values for the different data sets.

the amplitudes of the CMB angular power spectra  $C_l$  are proportional to the combination  $A_s e^{-2\tau}$ . Since the reionization history is closely coupled to the value of  $\tau$ , one anticipates that the inclusion of reionization-related data from quasar absorption spectra would affect the constraints on  $\tau$  and hence  $A_s$  and  $\sigma_8$ .

This **only-CMB** analysis will act as our baseline against which we will compare the rest of the analyses. In particular, these constraints will allow us to understand the effect of including reionization and 21 cm data in the next sections.

### 3.2 Joint constraints using CMB and quasar absorption data

Next, we include the reionization related observations from quasar absorption spectra in our analysis along with the Planck 2018 observations. The additional data sets related to reionization used for this analysis are described below:

(i) Measurements of the photoionization rate  $\Gamma_{\text{PI}}$  obtained from a combined analysis of quasar absorption spectra and hydrodynamical simulations (Becker & Bolton 2013; D’Aloisio et al. 2018; Calverley et al. 2011).

(ii) The redshift distribution of Lyman-limit system  $dN_{\text{LL}}/dz$  (Ribaud et al. 2011; O’Meara et al. 2013; Fumagalli et al. 2013;

Prochaska et al. 2010; Crighton et al. 2019; Songaila & Cowie 2010). To calculate  $dN_{\text{LL}}/dz$  from our model, we need to assume a functional form for the frequency distribution of the HI column density ( $N_{\text{HI}}$ ) and then have to integrate this function over all relevant  $N_{\text{HI}}$  values. The column density distribution has been taken from the latest compilation by Crighton et al. (2019). The lower limit of this integration depends on how one defines the Lyman-limit systems. For the  $2 < z < 5$ , the observational data points are taken from Crighton et al. (2019) where they have defined the Lyman-limit systems with  $N_{\text{HI}} \geq 10^{17.5} \text{ cm}^{-2}$ . Hence in this redshift range, we take the lower limit of the integration to be  $10^{17.5} \text{ cm}^{-2}$ . On the other hand, the observational point at  $z \sim 6$  has been taken from Songaila & Cowie (2010) where all systems with  $N_{\text{HI}} \geq 10^{17.2} \text{ cm}^{-2}$  are considered as Lyman-limit. Hence we have taken the lower limit of the integration to be  $10^{17.2} \text{ cm}^{-2}$  for  $z > 5$ .

(iii) The model independent upper limit on the neutral hydrogen fractions, measured from the dark fractions in quasar spectra (McGreer et al. 2015).

(iv) We also put a prior that reionization needs to be completed ( $Q_{\text{HII}} = 1$ ) at  $z \geq 5.3$ . This redshift constraint is motivated by studies of the large scale fluctuations of the effective Ly $\alpha$  optical depth from high redshift quasar spectra (Becker et al. 2015; Bosman

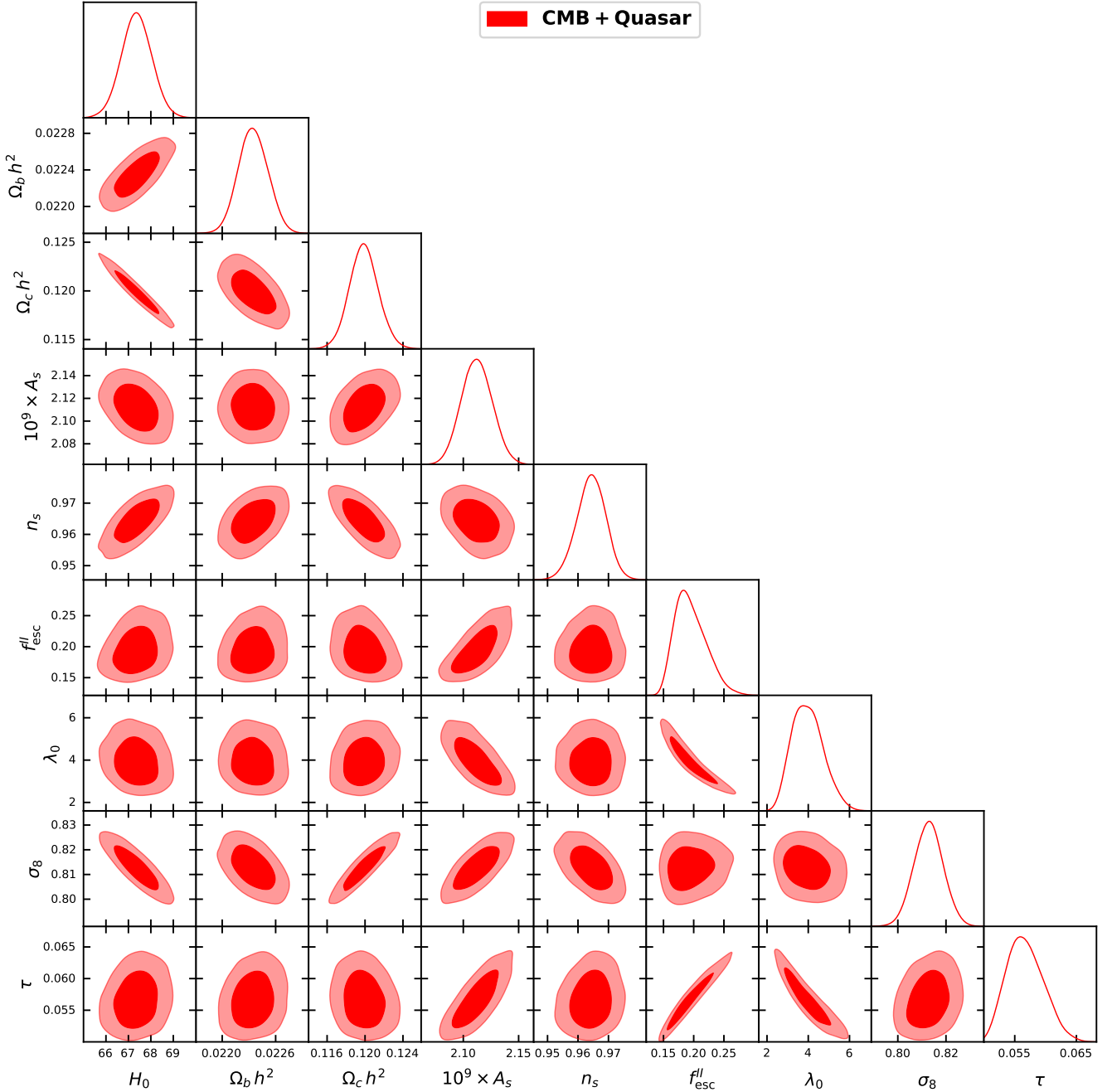


**Figure 2.** The marginalized posterior distribution of seven free parameters and two derived parameters ( $\sigma_8$  and  $\tau$ ) obtained for the **CMB+Quasar** case. We show the 68% and 95% confidence contours in the two-dimensional plots. Note that the posteriors for the cosmological parameters are identical to those for the **CMB+Quasar** case shown in Figure 1.

et al. 2018; Eilers et al. 2017, 2018). For example, using radiative transfer simulation, (Kulkarni et al. 2019a) predicts the completion of reionization to take place at redshift  $z \approx 5.3$ . Similarly, Choudhury et al. (2020) used a semi numerical approach to study the same and their model also predicted similar redshift for the completion of reionization.

The analysis procedure (referred as **CMB+Quasar** hereafter) is very similar to the **only-CMB** analysis. However, as we include the

reionization observations, the log-likelihood is modified to

$$\mathcal{L} = \mathcal{L}_{\text{Pl}} + \mathcal{L}_{\text{Re}}, \quad (21)$$

where

$$\mathcal{L}_{\text{Re}} = \frac{1}{2} \sum_{\alpha=1}^{N_{\text{obs}}} \left[ \frac{\zeta_{\alpha}^{\text{obs}} - \zeta_{\alpha}^{\text{th}}}{\sigma_{\alpha}} \right]^2. \quad (22)$$

Here  $\zeta_{\alpha}^{\text{obs}}$  represents the set of  $N_{\text{obs}}$  observational data related to photoionization rates and the distribution of the Lyman-Limit system



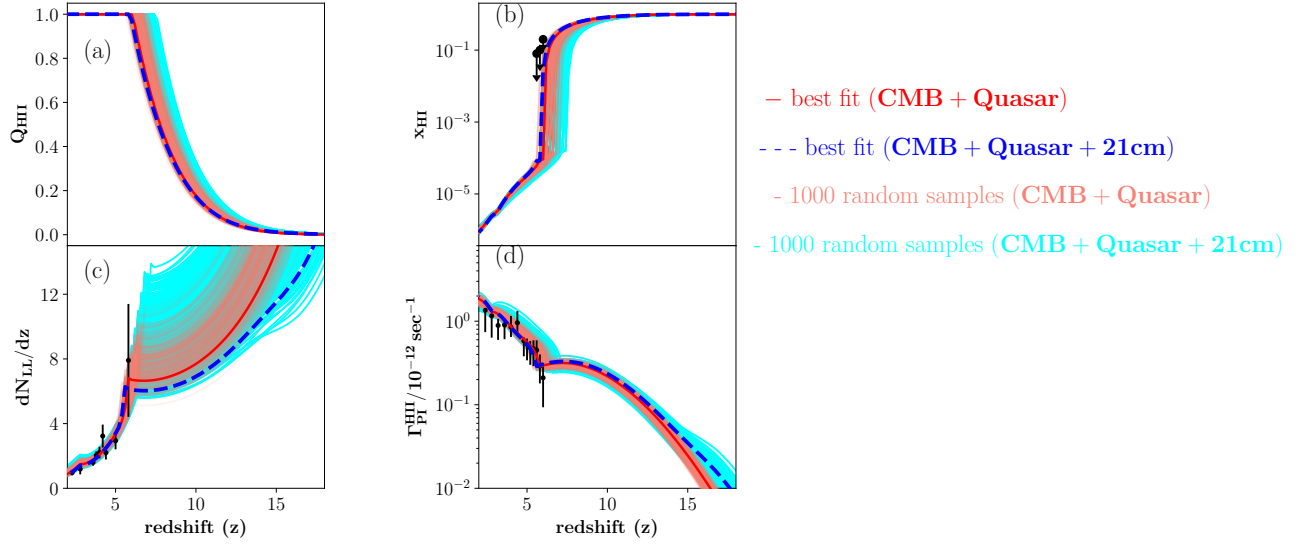


**Figure 3.** Redshift evolution of different quantities related to reionization for both **CMB+Quasar** and **CMB+Quasar+21cm** cases. In each panel, the light-red region show 1000 random samples obtained from the MCMC chains for the **CMB+Quasar** analysis whereas the red lines show the corresponding best-fit model. The cyan shaded region shows 1000 random samples for the **CMB+Quasar+21cm** analysis and the blue dashed curves show the corresponding best-fit curves. The different panels are: (a) The volume filling factor of HII region ( $Q_{\text{HII}}$ ). (b) The neutral hydrogen fraction ( $x_{\text{HI}}$ ). The black points with error-bars show the data points obtained from dark pixels fraction of Ly $\alpha$  absorption spectra (McGreer et al. 2015). (c) The redshift distribution of Lyman-limit system  $dN_{\text{LL}}/dz$ . The black points with error-bars show the observational data points (Songaila & Cowie 2010; Crighton et al. 2019). (d) The hydrogen photoionization rate ( $\Gamma_{\text{PI}}$ ). The black points with error bars are the observational data points (Calverley et al. 2011; Becker & Bolton 2013; D’Aloisio et al. 2018).

whereas  $\zeta_{\alpha}^{\text{th}}$  represents the values from the theoretical model. The  $\sigma_{\alpha}$  are the observational error bars.

The posterior distribution and the constraints on different parameters are shown in Figure 2. The mean and 95% confidence interval of the different parameters used in the analysis can be found in Table 1. The correlation between the cosmological parameters are similar to what is expected from any standard analysis of the CMB data. Some of the other interesting points of our analysis are as follows:

(i) There is a strong positive correlation between  $\tau$  and  $f_{\text{esc}}^{\text{II}}$ . This is obvious because as we increase the value of  $f_{\text{esc}}^{\text{II}}$  the reionization will take place earlier and as a result  $\tau$  will increase.

(ii) The free parameter  $\lambda_0$  shows a strong anti-correlation with  $\tau$  and  $f_{\text{esc}}^{\text{II}}$ . This is because while calculating  $\Gamma_{\text{PI}}$  in the CF model, the product  $\lambda_0 f_{\text{esc}}^{\text{II}}$  appears as a combination. This implies that, for a fixed value of  $\Gamma_{\text{PI}}$ , if  $f_{\text{esc}}^{\text{II}}$  is increased,  $\lambda_0$  has to decrease so as to keep their product fixed. As we have already discussed that  $f_{\text{esc}}^{\text{II}}$  is correlated with  $\tau$ , this immediately implies an anti-correlation between  $\tau$  and  $\lambda_0$ .

The constraints on the cosmological parameters are also shown in Figure 1, which allows a straightforward comparison with the previous **only-CMB** analysis. Similarly, one can also compare the obtained parameter limits for the two analyses from the respective columns in Table 1. Though the constraints on  $H_0$ ,  $\Omega_b h^2$ ,  $\Omega_c h^2$ ,  $n_s$  for the **CMB+Quasar** are not significantly different from the **only-CMB** analysis, the limits on  $\tau$ ,  $A_s$  and  $\sigma_8$  are different. Firstly, we note that the constraint on  $\tau$  is substantially tighter in **CMB+Quasar** analysis compared to that of **only-CMB**. This is a direct effect of including the quasar absorption observations in **CMB+Quasar** analysis. Lower values of  $\tau$ , which imply considerably delayed reionization,

are disallowed by the data points from dark pixels and also the prior that reionization needs to be completed before  $z = 5.3$ . On the other hand, higher values of  $\tau$  require higher values of  $f_{\text{esc}}^{\text{II}}$  and hence tend to produce a  $\Gamma_{\text{PI}}$  higher than allowed by the data. These two effects lead to a much restricted range in  $\tau$ . Now, we have already discussed in the previous section that  $A_s$  (or  $\sigma_8$ ) and  $\tau$  are correlated because of the dependence of  $C_l$  on them, hence a narrower posterior distribution in  $\tau$  will induce a similar change in  $A_s$  and  $\sigma_8$ . For example, the 95% C.L. for  $\sigma_8$  is  $\approx 0.023$  for the **CMB+Quasar** case, while it is  $\approx 0.032$  for the **only-CMB** case.

Figure 3 shows the redshift evolution of different quantities related to our reionization model: the ionized hydrogen fraction  $Q_{\text{HII}}$  (panel a), the neutral fraction  $x_{\text{HI}}$  (panel b), the redshift distribution of Lyman-limit systems  $dN_{\text{LL}}/dz$  (panel c) and the hydrogen photoionization rate  $\Gamma_{\text{PI}}$  (panel d). In all the panels, the red thick curves correspond to the best-fit model for the **CMB+Quasar** analysis whereas the light red region corresponds to 1000 random samples taken from the MCMC chains of this analysis. The black points are the observational data points. Our best-fit model agrees with the observational data points quite well. From panels (a) and (b), we see that the reionization starts around  $z \sim 12$  and is complete by redshift  $z \sim 5.5$ .

We also mention the best-fit log-likelihood values corresponding to different analyses in Table 1. We find that the value of the best-fit  $\mathcal{L}_{\text{PI}}$  (the Planck CMB likelihood) for the **CMB+Quasar** analysis is slightly higher than that of the **only-CMB**. This is because the best-fit model of the **only-CMB** analysis has a lower  $\tau$  than what is preferred by the quasar absorption data sets; in fact, the reionization ends later than what is implied by the dark pixel data. This too shows how

the inclusion of quasar absorption spectra affects the conclusions on allowed models.

#### 4 JOINT ANALYSIS USING CMB, QUASAR ABSORPTION AND 21 CM DATA

Next, for the first time, we include the 21 cm global signal data along with the CMB and reionization observations. Here we will discuss two scenarios, (i) we use a hypothetical 21 cm signal as a mock observation and (ii) we use the EDGES signal as the observations. The motivation behind doing the first analysis is that the EDGES signal requires including additional physics which leads to not so tight constraints on the cosmological parameters. The analysis with a hypothetical signal which is sensitive to reionization and does not require any additional physics allows us to demonstrate that using 21 cm signal could, in principle, be quite helpful in putting tighter constraints on cosmological parameters compared to **CMB+Quasar** analysis.

##### 4.1 CMB+Quasar+Hypothetical 21 cm signal

In this analysis, we include a mock data for the global 21 cm signal in addition to the CMB and Quasar data. The basic procedure for this scenario (**CMB+Quasar+21cm<sub>Pop-II</sub>** hereafter) is similar to that of **only-CMB** and **CMB+Quasar**. The construction of the hypothetical signal will depend on the source model assumed. For the sake of simplicity, while constructing the hypothetical signal, we assume contribution only from the usual PopII stars and ignore any contribution from PopIII. This allows efficient computation of the parameter posterior distributions and also easier interpretation of the results.

The inclusion of the 21 cm signal in our analysis requires computation of the same from the model which leads to an increase in the number of free parameters. As we are taking contributions only from PopII stars, the additional free parameters would be

- $f_{\alpha}^{\text{II}}$ : the normalization factor for the Ly $\alpha$  flux.
- $f_{Xh}^{\text{II}}$ : the heating efficiency of X-rays.

Thus, the nine free parameters for the joint analysis including the 21 cm signal are

$$\Theta = \{H_0, \Omega_b h^2, \Omega_c h^2, A_s, n_s, f_{\text{esc}}^{\text{II}}, \lambda_0, f_{Xh}^{\text{II}}, f_{\alpha}^{\text{II}}\}$$

In the presence of the mock 21 cm observations, the log-likelihood becomes

$$\mathcal{L} = \mathcal{L}_{\text{Pl}} + \mathcal{L}_{\text{Re}} + \mathcal{L}_{21, \text{PopII}}, \quad (23)$$

where  $\mathcal{L}_{21, \text{Pop-II}}$ , the loglikelihood corresponding to mock observational data is given by

$$\mathcal{L}_{21, \text{Pop-II}} = \sum_i \left[ \frac{\delta T_b^{\text{obs, PopII}}(v_i) - \delta T_b^{\text{th}}(v_i)}{\sigma_i} \right]^2, \quad (24)$$

where  $\delta T_b^{\text{obs, PopII}}(v_i)$  and  $\delta T_b^{\text{th}}(v_i)$  are the 21 cm differential brightness temperatures from the mock observational data and theoretical model, respectively and  $\sigma_i$  are the corresponding observational errors. The sum is over all frequency channels  $v_i$  of the mock data. We consider the frequency range 55–235 MHz, bin the signal into frequency channels of width 0.5 MHz. The mock data is generated using an assumed theoretical model (discussed in the next paragraph). In each bin, we add a Gaussian noise of zero mean and standard deviation  $\sigma_i = 10\text{mK}$  to the theoretical signal. This assumed value

of the standard deviation is moderately better than that found in the EDGES analysis which can be achieved by a longer integration. This lower value of  $\sigma_i$  is somewhat necessary to (i) detect the 21 cm emission signal during reionization (which is typically  $\sim 30\text{mK}$ ) and (ii) to put tighter constraints on cosmological parameters (compared to **CMB+Quasar**). With  $\sigma_i \approx 25\text{mK}$  (similar to EDGES), we find that varying the value of  $\sigma_8$  or other cosmological parameters within the Planck allowed limit does not have any significant effect in the 21 cm signal.

As the main purpose of this analysis is to check whether the inclusion of 21 cm signal puts any tighter constraints on the cosmological parameters compared to the **CMB+Quasar**, we use the same best-fit values coming from the earlier **CMB+Quasar** analysis for generating the mock data. The input values of other 21 cm related free parameters (which did not appear in the **CMB+Quasar** analysis) are taken as  $f_{Xh}^{\text{II}} = 0.2$  and  $f_{\alpha}^{\text{II}} = 1.0$ , consistent with the values estimated from the low redshift observations (Furlanetto et al. 2006).

Once the hypothetical 21 cm signal is constructed, we run an MCMC analysis to obtain the posterior distribution of all the nine parameters used in this analysis.

The constraints on the cosmological parameters are shown in Figure 4, which allows a straightforward comparison with the previous **CMB+Quasar** analysis. Though the constraints on  $H_0, \Omega_b h^2, \Omega_c h^2, n_s$  for the **CMB+Quasar+21cm<sub>Pop-II</sub>** are somewhat same as that of the **CMB+Quasar** analysis, the limits on  $\sigma_8, A_s, \tau$  are tighter. For example, we note that the constraint on  $\tau$  is now significantly tighter in the **CMB+Quasar+21cm<sub>Pop-II</sub>** analysis. The 95% C.L for  $\tau$  is  $\approx 0.005$  when 21 cm signal is added while it was  $\approx 0.01$  earlier. This is a direct effect of including the 21 cm observations. The reason is that in the later redshifts (i.e.,  $z \lesssim 9$ ), the 21 cm signal starts probing the reionization history. This effectively means that by including the 21 cm observations we are now constraining reionization history using three different observations - CMB, Quasar and 21 cm signal. Hence the constraint on  $\tau$  would be more stringent once the 21 cm signal is included. And, as it is well known that  $\tau$  and  $A_s$  (or  $\sigma_8$ ) are correlated, the change in  $\tau$  will also induce the change in the constraint of  $\sigma_8$ .

Interestingly, the fact that constraining  $\tau$  from 21 cm experiments would lead to better limits on the cosmological parameters was already noted by Liu & Parsons (2016) and Liu et al. (2016). For example, in Liu & Parsons (2016), the authors have used combination of Planck observations, mock 21 cm power spectrum, and a mock global 21 cm signal to constrain both the astrophysical and cosmological parameters and found a tighter constraints on them. However, they consider only a small portion of the 21 cm signal (in the redshift range when the spin temperature is much larger compared to the background radiation temperature  $T_\gamma$ , i.e.,  $T_s \gg T_\gamma$ ). For this simplification, they did not have to introduce any extra parameters related to 21 cm signal. Also, unlike us, they did not consider any reionization related observations in their analysis.

The posterior distribution and the constraints on different parameters for the **CMB+Quasar+21cm<sub>Pop-II</sub>** analysis are shown in Figure 5. The correlation between the cosmological parameters are similar to what is expected from any standard analysis of the CMB data. The other interesting points of our analysis are as follows

- (i) There is a strong anti correlation between  $\sigma_8 - f_{Xh}^{\text{II}}$  and  $\sigma_8 - f_{\alpha}^{\text{II}}$ . This is expected as we increase the value of  $\sigma_8$ , the structure formation will start earlier and the only way to keep the 21 cm signal unchanged is to decrease the efficiency of Ly $\alpha$  photon production (controlled by  $f_{\alpha}^{\text{II}}$ ) and X-ray photon production (controlled by  $f_{Xh}^{\text{II}}$ ).
- (ii) We also note a strong positive correlation between  $f_{Xh}^{\text{II}}$  and

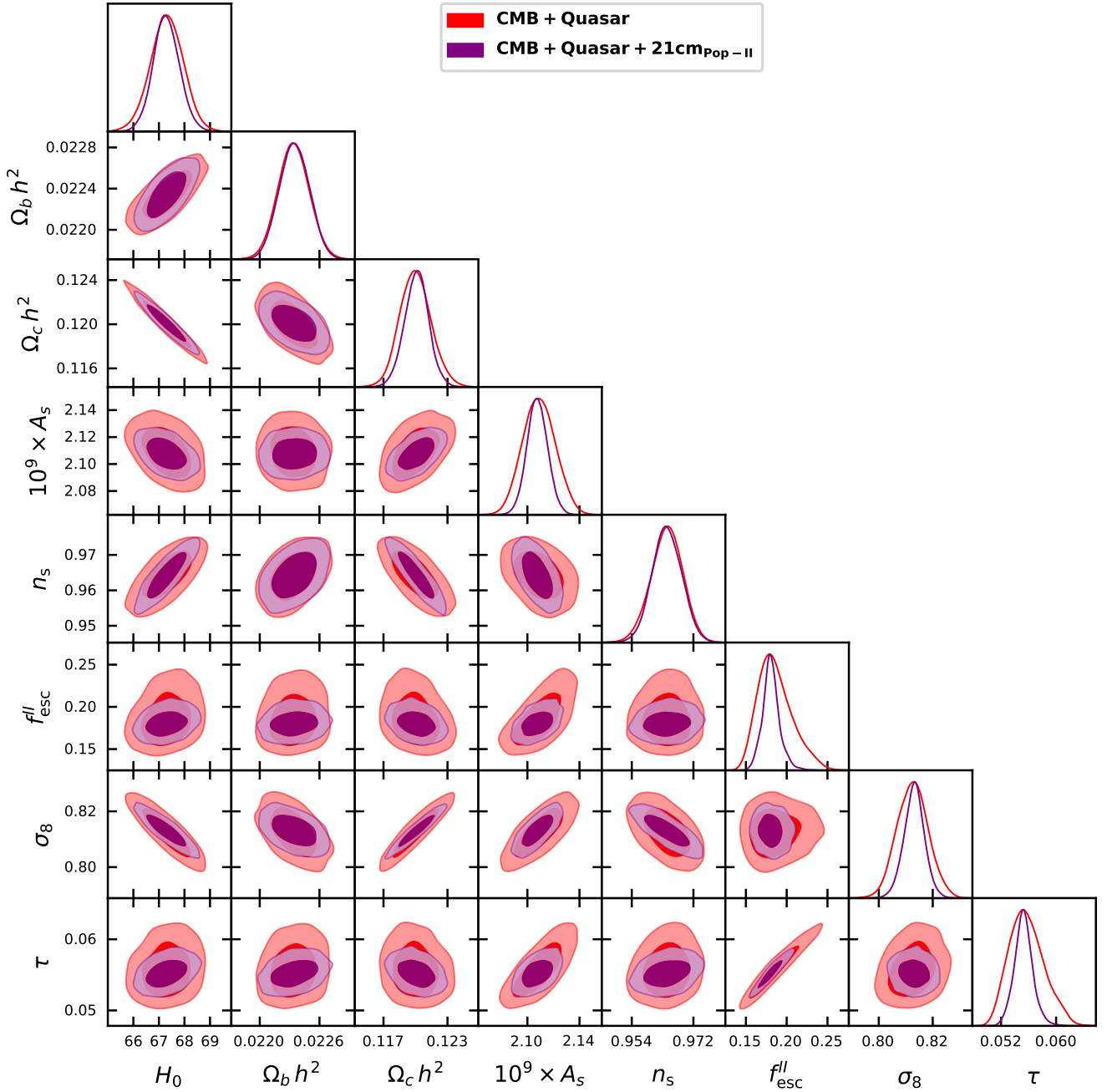


**Figure 4.** The marginalized posterior distributions of cosmological parameters obtained from **CMB+Quasar** (red) and **CMB+Quasar+21cm<sub>Pop-II</sub>** (purple) analyses. We show the 68% and 95% confidence contours in the two-dimensional plots. Note that  $\sigma_8$  and  $\tau$  are derived parameters while the others are free parameters in our model.

$f_{\alpha}^{\text{II}}$ . This is also expected because increasing the Ly- $\alpha$  photon production efficiency will lead to a deeper absorption trough in the 21 cm signal and the only way to keep the minima of the signal unaltered is to increase the X-ray heating efficiency (which is determined by  $f_{\text{Xh}}^{\text{II}}$ ).

We also show a comparison between the mock data (black line with error bars) and the 21 cm signal recovered from the MCMC analysis for this case in Figure 6. The cyan shaded region shows the 1000 random samples from the MCMC chains and the purple curve

corresponds to the best fit-values of the free parameters. It is evident from the figure that the recovered model matches quite well with the mock observation.

#### 4.2 CMB+Quasar+EDGES signal

Next, we describe the scenario where the EDGES 21 cm observation is included in our analysis. The basic analysis procedure for this scenario (**CMB+Quasar+21cm** hereafter) is very similar to

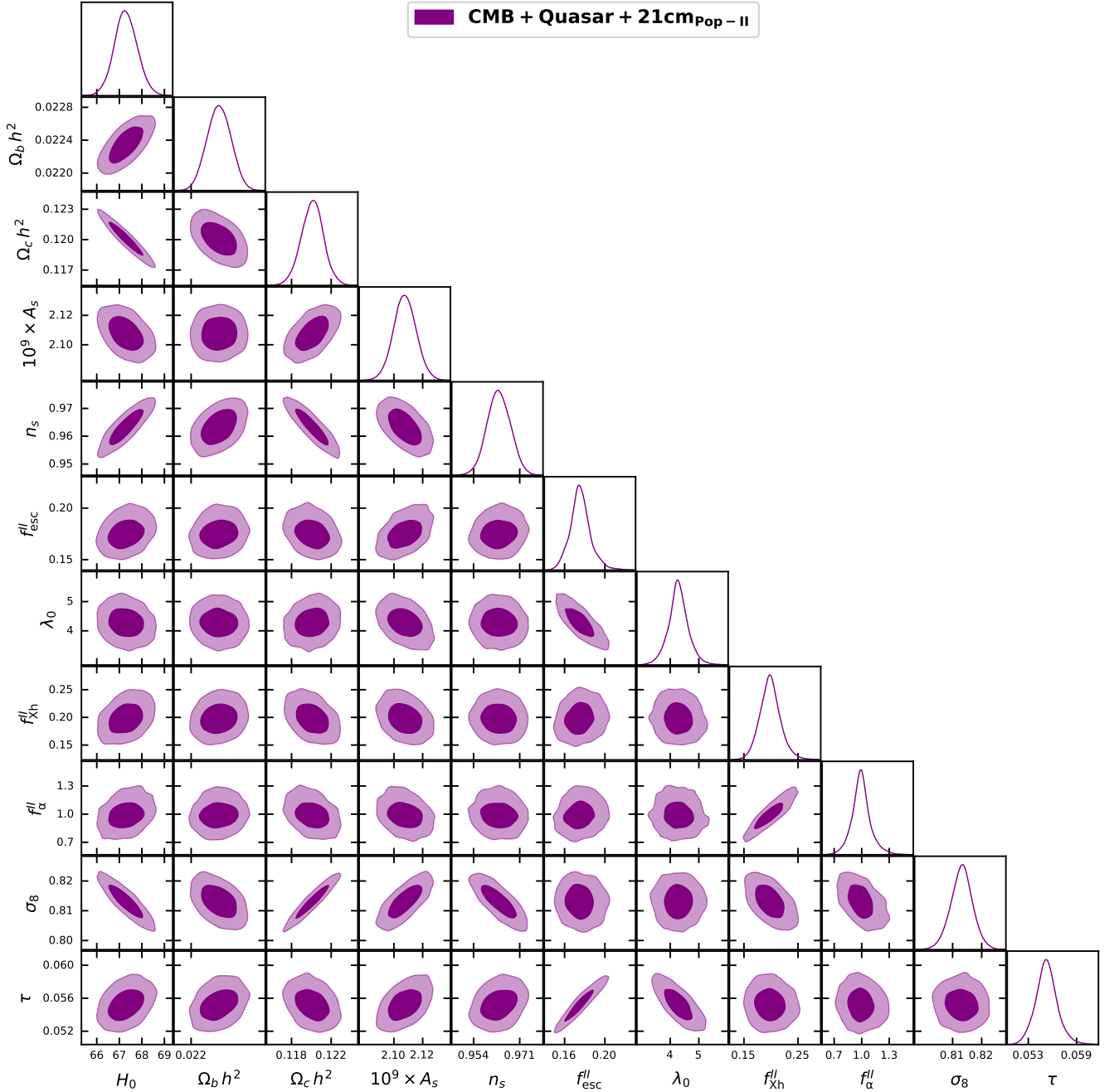


**Figure 5.** The marginalized posterior distribution of nine free parameters and two derived parameters ( $\sigma_8$  and  $\tau$ ) obtained for the **CMB+Quasar+21cm<sub>Pop-II</sub>** case. We show the 68% and 95% confidence contours in the two-dimensional plots. Note that the posteriors for the cosmological parameters are identical to those for the **CMB+Quasar+21cm<sub>Pop-II</sub>** case shown in Figure 4.

that of **CMB+Quasar+21cm<sub>Pop-II</sub>**. The main differences are that we include the contribution of PopIII stars in **CMB+Quasar+21cm** analysis and an excess radio contribution has been considered here. As we will see, they are crucial in explaining the 21 cm data from EDGES.

For the PopIII stars, the first point to note is that it is not straightforward to fix the value of star-forming efficiency  $f_*^{\text{III}}$  (recall that for PopII stars, we fixed it using the observations of the UV luminosity function at  $z \sim 6 - 10$ ). However, this is not a serious obstacle as

$f_*^{\text{III}}$  appears as multiplicative factors with other free parameters and hence can be absorbed within them appropriately. Hence the free parameters for PopIII are

- $f_{*,\text{esc}}^{\text{III}} \equiv f_*^{\text{III}} f_{\text{esc}}^{\text{III}}$ : the escape of photons into the IGM.
- $f_{*,\alpha}^{\text{III}} \equiv f_*^{\text{III}} f_{\alpha}^{\text{III}}$ : the Ly $\alpha$  flux.
- $f_{*,Xh}^{\text{III}} \equiv f_*^{\text{III}} f_{Xh}^{\text{III}}$ : the heating efficiency of X-rays.
- $f_{*,R}^{\text{II}} \equiv f_*^{\text{III}} f_R^{\text{III}}$ : the radio-SFR relation.
- $z_{\text{trans}}$ : the transition redshift for PopIII  $\rightarrow$  PopII stars.

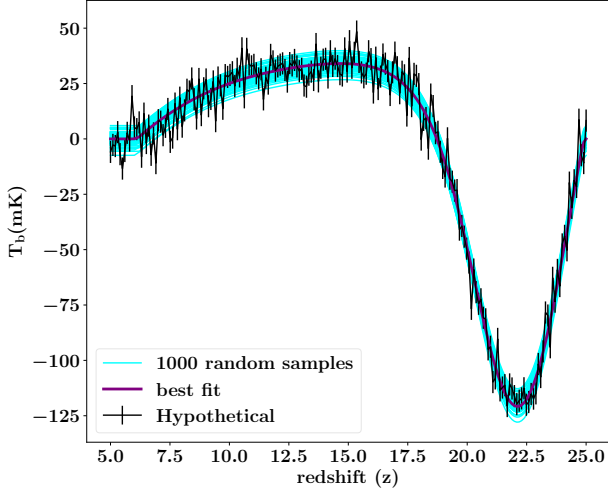


**Figure 6.** Comparison between the mock observations and the 21 cm signal recovered from our MCMC analysis in the **CMB+Quasar+21cm<sub>Pop-II</sub>** case. The purple curve shows the best-fit model whereas the cyan curves show 1000 random samples from the MCMC chains. The black line with the error bars represents the mock data points. Our recovered signal matches quite well with the mock data.

Hence a joint analysis of all the data sets requires varying fifteen parameters (seven parameters of the earlier analyses and eight new parameters) simultaneously. This is an enormously challenging task which requires enormous computing time. We can simplify the analysis using some insights gained in our earlier work (Chatterjee et al. 2020). It has been shown that it is sufficient to vary only the five parameters:  $f_{Xh}^{\text{II}}$ ,  $f_{*,\text{esc}}^{\text{III}}$ ,  $f_{*,\alpha}^{\text{III}}$ ,  $f_{*,R}^{\text{III}}$ ,  $z_{\text{trans}}$  in order to explain the EDGES signal. For the other four parameters related to the 21 cm signal, we assume the following: we fix  $f_{\alpha}^{\text{II}} = f_R^{\text{II}} = 1$  which is equivalent to assuming that the Ly $\alpha$  and radio properties of the PopII stars remain similar to what is observed at lower redshifts. In addition, Chatterjee et al. (2020) showed that the X-ray heating contribution of the PopIII stars is negligible compared to the PopII, so we take  $f_{Xh}^{\text{III}} = 0$ . In Chatterjee et al. (2020), we found that the  $z \leq 16$  part of the 21 cm signal is dominated by the X-ray heating whereas the  $z \geq 16$  is dominated by excess radio background and Lyman- $\alpha$  background. Chatterjee et al. (2020) also suggest that for the  $z \leq 16$  part of the 21 cm signal, contribution comes mostly from PopII stars and not from PopIII stars. Hence, even if we consider X-ray contribution from PopIII, the match with the data would remain the same but at an expense of adding one more free parameter in the MCMC analysis.

So, the twelve free parameters for the joint analysis including the 21 cm signal are

$$\Theta = \{H_0, \Omega_b h^2, \Omega_c h^2, A_s, n_s, f_{\text{esc}}^{\text{II}}, \lambda_0, f_{Xh}^{\text{II}}, f_{*,\text{esc}}^{\text{III}}, f_{*,\alpha}^{\text{III}}, f_{*,R}^{\text{III}}, z_{\text{trans}}\}$$

In the presence of the EDGES observations, the log-likelihood becomes

$$\mathcal{L} = \mathcal{L}_{\text{Pl}} + \mathcal{L}_{\text{Re}} + \mathcal{L}_{21}, \quad (25)$$

where  $\mathcal{L}_{21}$  is given by

$$\mathcal{L}_{21} = \sum_i \left[ \frac{\delta T_b^{\text{obs}}(v_i) - \delta T_b^{\text{th}}(v_i)}{\sigma_i} \right]^2, \quad (26)$$

where  $\delta T_b^{\text{obs}}(v_i)$  and  $\delta T_b^{\text{th}}(v_i)$  are the 21 cm differential brightness temperatures from the observational data and theoretical model respectively and  $\sigma_i$  are the observational errors. The sum is over all frequency channels  $v_i$  of the EDGES data. We take  $\sigma_i = 25\text{mK}$ , consistent with Hills et al. (2018).

The posterior distributions of the different parameters are shown in Figure 7. The corresponding values can be found in Table 1. The first point to note is that the efficiency parameters related to the PopIII stars are required to be non-zero to match the data. We also find that the transition redshift  $z_{\text{trans}}$  is well constrained between 15.89 and 16.68, thus clearly indicating that the PopIII stars must cease to exist around  $z \sim 16$ . This is consistent with the findings of Chatterjee et al. (2020). Also, since the PopIII contribution terminates at such a high redshift, our model will automatically be less than the excess radio background allowed by the ARCADE-2 observations (Fixsen et al. 2011). Previously, other studies Reis et al. (2020); Chatterjee et al. (2019) too have found that the radio background must be turned off at  $z \sim 16$ . We require a large value of  $f_{*,R}^{\text{III}}$  ( $\approx 10^4$ ) suggesting a highly efficient radio emission from the PopIII stars. Interestingly, Reis et al. (2020) have also found a similar value for this quantity while studying the effect of inhomogeneous radio background (coming from a population of high-redshift galaxies) in both 21 cm power spectrum and the global signal.

Another interesting feature to note from this figure is a very strong correlation between  $f_{*,R}^{\text{III}}$  and  $f_{Xh}^{\text{II}}$ . This is expected because higher the radio background, deeper will be the absorption trough of the 21 cm signal around  $z_{\text{trans}}$ . However, the observed signal approaches zero at redshift  $z \sim 14$  and the only way to match with this feature is to add more X-ray heating.

As far as the reionization history is concerned, we find that  $\tau$  is correlated with  $f_{\text{esc}}^{\text{II}}$  and is anti-correlated with  $\lambda_0$ , similar to the **CMB+Quasar** analysis. However we see that there is no correlation between  $\tau$  and  $f_{*,\text{esc}}^{\text{III}}$ , thus implying that the reionization history is not sensitive to the details of the PopIII stars. There are some differences in the posterior distributions of  $H_0$ ,  $\Omega_b h^2$  and  $\Omega_c h^2$ , however, these are not statistically significant at this stage.

In Figure 1, we compare the constraints on the cosmological parameters for the **CMB+Quasar+21cm** with the earlier analyses **only-CMB** and **CMB+Quasar**. As can be seen, the constraints for the **CMB+Quasar+21cm** are almost identical to the **CMB+Quasar**, thus implying that the EDGES data do not have any significant effect on the cosmological parameters of the  $\Lambda\text{CDM}$  model. The **CMB+Quasar+21cm** prefers slightly higher values of  $\tau$  compared to **only-CMB** analysis, driven by the presence of PopIII stars.

The redshift evolution of different reionization-related quantities has been compared with the **CMB+Quasar** in Figure 3. The dashed blue lines show the best-fit results of **CMB+Quasar+21cm** analysis whereas the cyan regions correspond to 1000 random samples taken from the MCMC chains. We find that the **CMB+Quasar+21cm** analysis prefers somewhat earlier reionization which is the result of including the PopIII stars in the model. We also find that the **CMB+Quasar+21cm** allows a wider range of reionization histories compared to **CMB+Quasar** which too is a consequence of including additional free parameters. The best-fit models for the two cases, however, are almost identical which can also be seen from the parameter values in Table 1 along with the corresponding log-likelihood values.

Finally, we show the comparison between the EDGES data and the 21 cm signal obtained from the MCMC analysis in Figure 8. The cyan shaded region shows 1000 random samples from the MCMC chains and the blue curve corresponds to the best-fit values of the free parameters. Though the amplitude of the absorption matches with



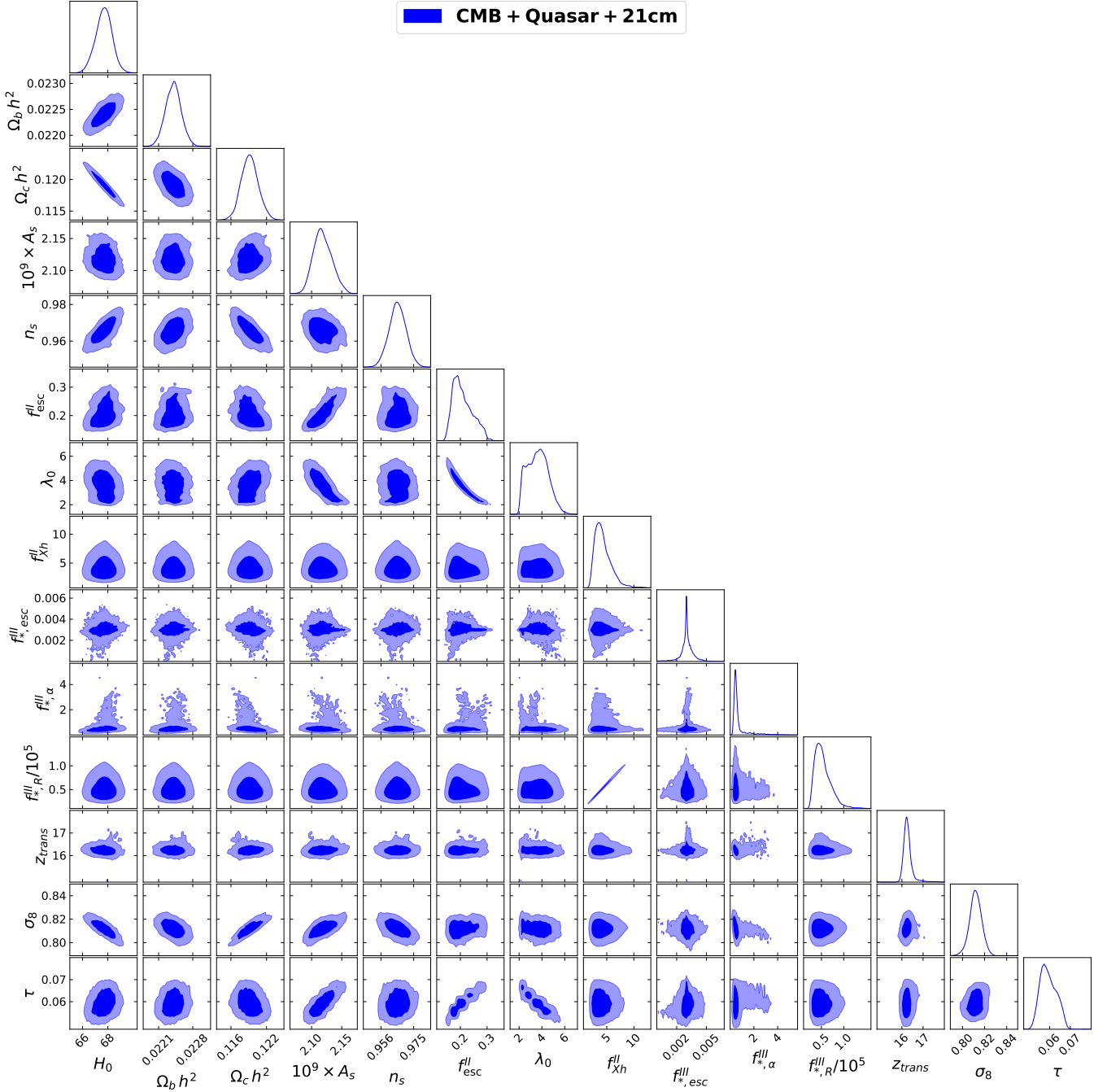


**Figure 7.** The marginalized posterior distribution of twelve free parameters and two derived parameters ( $\sigma_8$  and  $\tau$ ) obtained for the **CMB+Quasar+21cm** case. We show the 68% and 95% confidence contours in the two-dimensional plots. Note that the posteriors for the cosmological parameters are identical to those for the **CMB+Quasar+21cm** case shown in Figure 1.

the observations, our theoretical model cannot produce the “flat-bottom” shape as seen in the observed signal. Chatterjee et al. (2020) has shown that to reproduce this shape, one needs to employ a much more complicated shape for the PopIII star formation, e.g., a fourth-order log-polynomial. This would naturally lead to a significantly more model parameters which we postpone to a later work.

## 5 CONCLUSION AND DISCUSSION

In this work, we introduce CosmoReionMC, an advanced Markov Chain Monte Carlo (MCMC) based parameter estimation package using a variety of cosmological and reionization-related observations. In particular, we include the 21 cm global signal from cosmic dawn in the analysis. To our knowledge, this is the first time the 21 cm data has been combined with the cosmological observations.

Our formalism is based on (i) a reionization model developed by Choudhury & Ferrara (2005, 2006) with improvements by Mitra

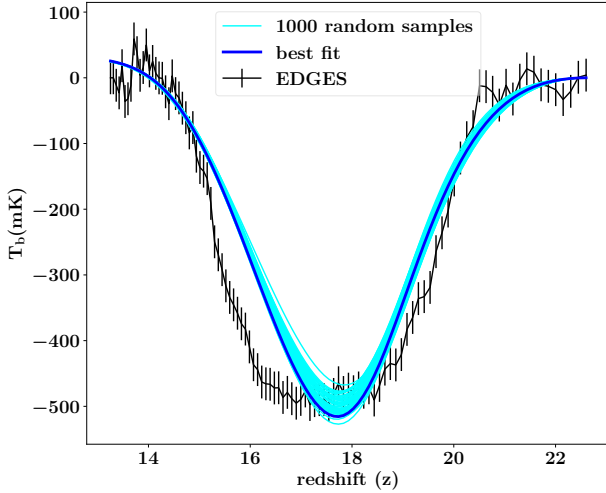


**Figure 8.** Comparison between EDGES observations (Bowman et al. 2018) and the 21 cm signal recovered from our MCMC analysis in the **CMB+Quasar+21cm** case. The blue curve shows the best-fit model while as the cyan curves show 1000 random samples from the MCMC chains. The black line with the error bars represents the EDGES data points. Our model can match the position and depth of the EDGES absorption trough, however, matching the exact shape would require more complex evolution of the PopIII star formation than what is assumed in this paper.

et al. (2011), (ii) a model for 21 cm signal based on Furlanetto (2006); Crighton et al. (2019) and (iii) a publicly available package CAMB (Lewis 2013) for computing the CMB anisotropies, modified to account for arbitrary reionization histories. The code is then coupled to a MCMC code emcee (Foreman-Mackey et al. 2013) to compute the posteriors of the free parameters.

Depending on the data sets used, we perform three different analyses with our package:

(i) **only-CMB:** We use only Planck2018 CMB anisotropy data in this analysis. Compared to the conventional analyses of the CMB data, this is equivalent to replacing the parameterized reionization history (either tanh or more advanced parametrization) with a physically motivated reionization model. We find that the bounds on the cosmological parameters are similar to what is obtained in the conventional tanh parameterization of reionization history.

(ii) **CMB+Quasar:** In this analysis we include the reionization-related observations based on quasar absorption spectra, namely, the constraints on the hydrogen photoionization rate (Calverley et al. 2011; Becker & Bolton 2013; D’Aloisio et al. 2018), the redshift distribution of the Lyman-limit systems (Songaila & Cowie 2010; Crighton et al. 2019), the model-independent constraints using the dark pixels (McGreer et al. 2015) and prior on the end of reionization based on the Ly $\alpha$  opacity fluctuations (Kulkarni et al. 2019a; Choudhury et al. 2020). The inclusion of these observations lead to much tighter constraints on  $\tau$  compared to **only-CMB** analysis which, in turn, lead to tighter constraints on the amplitude of the primordial power spectrum  $A_s$  and  $\sigma_8$ .

(iii) **CMB+Quasar+21cm:** In this case we add the EDGES observations of 21 cm global signal (Bowman et al. 2018) along with the CMB and quasar absorption data. The main difference of this analysis with the earlier ones is that the EDGES data requires a radio-

efficient short-lived population of metal-free (PopIII) stars which give rise to the absorption trough. The inclusion of the PopIII stars allow reionization histories that start earlier than what is found in the **CMB+Quasar** analysis. With the present EDGES data, the constraints on the cosmological parameters are very similar in the two cases.

There are a couple of caveats worth highlighting here. Our analysis assumes all the efficiency parameters related to the PopII and PopIII stars to be redshift-independent, which is clearly too simplistic. In fact, several studies suggest that they are possibly function of halo masses and redshifts. For the reionization-related data, the only parameter which is of relevance is  $N_{\text{ion}}$ , see equation (3), which is a multiplication of several physical parameters including  $f_*$  and  $f_{\text{esc}}$ . In such cases, it is possible to treat  $N_{\text{ion}}$  as an arbitrary function of  $z$  and constrain its evolution using Principal Component Analysis (Mitra et al. 2011). Similarly, one can also include halo mass-dependence using some simple power-law parameterization (see e.g., Yung et al. 2019; Kimm et al. 2019; Paardekooper et al. 2015; Ferrara & Loeb 2013). Inclusion of the 21 cm data, however, introduces additional efficiency parameters related to the Ly $\alpha$  radiation, X-ray heating and the radio background. In such a scenario, implementing  $z$  and  $M$ -dependent efficiency parameters would lead to a significantly larger number of free parameters thus making the parameter estimation exceedingly challenging. Such issues will be explored elsewhere.

The second point to keep in mind is that the origin and amplitude of the EDGES 21 cm signal is still highly debated (see, e.g., Hills et al. 2018; Sims & Pober 2020). In case the amplitude of the signal is found to be less than what is currently claimed, the need for an excess radio background and hence the need for introducing PopIII stars in the model will go away. Whether this will have any effect on the cosmological parameters needs to be investigated.

The CosmoReionMC package can be extended to study different kinds of problems. For example, it is straightforward to include other cosmological data sets (say, BAO) in the analysis. On the astrophysical side too, we can include other constraints on the reionization history. The package can also be used to probing non-standard extensions to the standard  $\Lambda$ CDM model, e.g., evolving dark energy and light dark matter particles. Similarly, newer measurements of the 21 cm global signal are expected from several other experiments aiming to detect it, e.g., the Shaped Antenna measurement of the background Radio Spectrum (SARAS, Patra et al. 2013; Singh et al. 2017), the Large-Aperture Experiment to Detect the Dark Ages (LEDA, Greenhill & Bernardi 2012), SCI-HI (Voytek et al. 2014), the Broadband Instrument for Global Hydrogen Reionisation Signal (BIGHORNS, Sokolowski et al. 2015), and the Cosmic Twilight Polarimeter (CTP, Nhan et al. 2018). It would be interesting to check if these measurements have any impact on the cosmological and reionization parameters. Such possibilities will be explored in the future. In addition, we are also planning to make CosmoReionMC public in the near future.

To summarise, the CosmoReionMC is a unique parameter estimation package which can probe cosmological and astrophysical parameters related to reionization simultaneously using a wide variety of data sets. This should have many interesting applications in the future.

## ACKNOWLEDGEMENTS

We thank the anonymous referee for their helpful and constructive comments on the first version of the paper. AC and TRC acknowledge support of the Department of Atomic Energy, Government of India,

under project no. 12-R&D-TFR-5.02-0700. TRC is also supported by the Associateship Scheme of ICTP.

## DATA AVAILABILITY

The observational data used here are taken from literature and the code underlying this article will be shared on reasonable request to the corresponding author.

## REFERENCES

- Akeret J., Seehars S., Amara A., Refregier A., Csillaghy A., 2013, *Astronomy and Computing*, **2**, 27
- Barkana R., Loeb A., 2001, *Phys. Rep.*, **349**, 125
- Barkana R., Outmezguine N. J., Redigol D., Volansky T., 2018, *Phys. Rev. D*, **98**, 103005
- Becker G. D., Bolton J. S., 2013, *MNRAS*, **436**, 1023
- Becker G. D., Bolton J. S., Madau P., Pettini M., Ryan-Weber E. V., Venemans B. P., 2015, *MNRAS*, **447**, 3402
- Bosman S. E. I., Fan X., Jiang L., Reed S., Matsuoaka Y., Becker G., Haehnelt M., 2018, *MNRAS*, **479**, 1055
- Bouwens R. J., Illingworth G. D., Blakeslee J. P., Franx M., 2006, *ApJ*, **653**, 53
- Bouwens R. J., et al., 2015, *ApJ*, **803**, 34
- Bowman J. D., Rogers A. E. E., Monsalve R. A., Mozdzen T. J., Mahesh N., 2018, *Nature*, **555**, 67
- Bradley R. F., Tauscher K., Rapetti D., Burns J. O., 2019, *ApJ*, **874**, 153
- Bromm V., Loeb A., 2003, *Nature*, **425**, 812
- Bruzual G., Charlot S., 2003, *MNRAS*, **344**, 1000
- Calverley A. P., Becker G. D., Haehnelt M. G., Bolton J. S., 2011, *MNRAS*, **412**, 2543
- Chatterjee A., Dayal P., Choudhury T. R., Hutter A., 2019, *MNRAS*, **487**, 3560
- Chatterjee A., Dayal P., Choudhury T. R., Schneider R., 2020, *MNRAS*, **496**, 1445
- Chiu W. A., Ostriker J. P., 2000, *ApJ*, **534**, 507
- Choudhury T. R., 2009, *Current Science*, **97**, 841
- Choudhury T. R., Ferrara A., 2005, *MNRAS*, **361**, 577
- Choudhury T. R., Ferrara A., 2006, *MNRAS*, **371**, L55
- Choudhury T. R., Paranjape A., Bosman S. E. I., 2020, arXiv e-prints, p. arXiv:2003.08958
- Crighton N. H. M., Prochaska J. X., Murphy M. T., O’Meara J. M., Worseck G., Smith B. D., 2019, *MNRAS*, **482**, 1456
- D’Aloisio A., McQuinn M., Davies F. B., Furlanetto S. R., 2018, *MNRAS*, **473**, 560
- Davies J. E., Mutch S. J., Qin Y., Mesinger A., Poole G. B., Wyithe J. S. B., 2019, *MNRAS*, **489**, 977
- Dayal P., Ferrara A., 2018, *Phys. Rep.*, **780**, 1
- Douspis M., Aghanim N., Ilić S., Langer M., 2015, *A&A*, **580**, L4
- Eilers A.-C., Davies F. B., Hennawi J. F., Prochaska J. X., Lukić Z., Mazzucchelli C., 2017, *ApJ*, **840**, 24
- Eilers A.-C., Davies F. B., Hennawi J. F., 2018, *ApJ*, **864**, 53
- Ewall-Wice A., Chang T. C., Lazio J., Doré O., Seiffert M., Monsalve R. A., 2018, *ApJ*, **868**, 63
- Ewall-Wice A., Chang T.-C., Lazio T. J. W., 2020, *MNRAS*, **492**, 6086
- Feng C., Holder G., 2018, *ApJ*, **858**, L17
- Ferrara A., Loeb A., 2013, *MNRAS*, **431**, 2826
- Fialkov A., Barkana R., 2019, *MNRAS*, **486**, 1763
- Fialkov A., Barkana R., Visbal E., Tselikhovich D., Hirata C. M., 2013, *MNRAS*, **432**, 2909
- Field G. B., 1958, *Proceedings of the IRE*, **46**, 240
- Fixsen D. J., et al., 2011, *ApJ*, **734**, 5
- Foreman-Mackey D., Hogg D. W., Lang D., Goodman J., 2013, *PASP*, **125**, 306
- Fraser S., et al., 2018, *Physics Letters B*, **785**, 159
- Fumagalli M., O’Meara J. M., Prochaska J. X., Worseck G., 2013, *ApJ*, **775**, 78
- Furlanetto S. R., 2006, *MNRAS*, **371**, 867
- Furlanetto S. R., Oh S. P., Briggs F. H., 2006, *Phys. Rep.*, **433**, 181
- Ghara R., Mellema G., 2020, *MNRAS*, **492**, 634
- Ghara R., Giri S. K., Ciardi B., Mellema G., Zaroubi S., 2021, *MNRAS*, **503**, 4551
- Gillet N., Mesinger A., Greig B., Liu A., Ucci G., 2019, *MNRAS*, **484**, 282
- Greenhill L. J., Bernardi G., 2012, arXiv e-prints, p. arXiv:1201.1700
- Greig B., Mesinger A., 2015, *MNRAS*, **449**, 4246
- Greig B., Mesinger A., 2017a, *MNRAS*, **465**, 4838
- Greig B., Mesinger A., 2017b, *MNRAS*, **472**, 2651
- Greig B., Mesinger A., 2018, *MNRAS*, **477**, 3217
- Greig B., Mesinger A., Koopmans L. V. E., 2020, *MNRAS*, **491**, 1398
- Haiman Z., Rees M. J., Loeb A., 1997, *ApJ*, **476**, 458
- Hassan S., Davé R., Finlator K., Santos M. G., 2017, *MNRAS*, **468**, 122
- Hazra D. K., Smoot G. F., 2017, *J. Cosmology Astropart. Phys.*, **2017**, 028
- Hazra D. K., Paoletti D., Finelli F., Smoot G. F., 2020, *Phys. Rev. Lett.*, **125**, 071301
- Hills R., Kulkarni G., Meerburg P. D., Puchwein E., 2018, *Nature*, **564**, E32
- Hu W., 2000, *ApJ*, **529**, 12
- Hu W., Dodelson S., 2002, *ARA&A*, **40**, 171
- Hu W., Holder G. P., 2003, *Phys. Rev. D*, **68**, 023001
- Hutter A., Dayal P., Yepes G., Gottlöber S., Legrand L., Ucci G., 2020, arXiv e-prints, p. arXiv:2004.08401
- Ishigaki M., Kawamata R., Ouchi M., Oguri M., Shimasaku K., Ono Y., 2018, *ApJ*, **854**, 73
- Jaacks J., Thompson R., Finkelstein S. L., Bromm V., 2018, *MNRAS*, **475**, 4396
- Katz H., Kimm T., Haehnelt M. G., Sijacki D., Rosdahl J., Blaizot J., 2019, *MNRAS*, **483**, 1029
- Kern N. S., Liu A., Parsons A. R., Mesinger A., Greig B., 2017, *ApJ*, **848**, 23
- Kimm T., Katz H., Haehnelt M., Rosdahl J., Devriendt J., Slyz A., 2017, *MNRAS*, **466**, 4826
- Kimm T., Blaizot J., Garel T., Michel-Dansac L., Katz H., Rosdahl J., Verhamme A., Haehnelt M., 2019, *MNRAS*, **486**, 2215
- Kulkarni G., Keating L. C., Haehnelt M. G., Bosman S. E. I., Puchwein E., Chardin J., Aubert D., 2019a, *MNRAS*, **485**, L24
- Kulkarni G., Worseck G., Hennawi J. F., 2019b, *MNRAS*, **488**, 1035
- Lesgourgues J., 2011, arXiv e-prints, p. arXiv:1104.2932
- Lewis A., 2008, *Phys. Rev. D*, **78**, 023002
- Lewis A., 2013, *Phys. Rev. D*, **87**, 103529
- Liu A., Parsons A. R., 2016, *MNRAS*, **457**, 1864
- Liu A., Pritchard J. R., Allison R., Parsons A. R., Seljak U., Sherwin B. D., 2016, *Phys. Rev. D*, **93**, 043013
- Livermore R. C., Finkelstein S. L., Lotz J. M., 2017, *ApJ*, **835**, 113
- Loeb A., Barkana R., 2001, *ARA&A*, **39**, 19
- Maio U., Ciardi B., Dolag K., Tornatore L., Khochfar S., 2010, *MNRAS*, **407**, 1003
- Maio U., Khochfar S., Johnson J. L., Ciardi B., 2011, *MNRAS*, **414**, 1145
- McGreer I. D., Mesinger A., D’Odorico V., 2015, *MNRAS*, **447**, 499
- McQuinn M., Furlanetto S. R., Hernquist L., Zahn O., Zaldarriaga M., 2005, *ApJ*, **630**, 643
- Mebane R. H., Mirocha J., Furlanetto S. R., 2020, *MNRAS*, **493**, 1217
- Mesinger A., Greig B., Sobacchi E., 2016, *MNRAS*, **459**, 2342
- Mineo S., Gilfanov M., Sunyaev R., 2012, *MNRAS*, **419**, 2095
- Miralda-Escudé J., 2003, *ApJ*, **597**, 66
- Miranda V., Lidz A., Heinrich C. H., Hu W., 2017, *MNRAS*, **467**, 4050
- Mirocha J., Furlanetto S. R., 2019, *MNRAS*, **483**, 1980
- Mitra S., Choudhury T. R., Ferrara A., 2011, *MNRAS*, **413**, 1569
- Mitra S., Choudhury T. R., Ferrara A., 2012, *MNRAS*, **419**, 1480
- Mitra S., Ferrara A., Choudhury T. R., 2013, *MNRAS*, **428**, L1
- Mitra S., Choudhury T. R., Ferrara A., 2015, *MNRAS*, **454**, L76
- Mitra S., Choudhury T. R., Ferrara A., 2018a, *MNRAS*, **473**, 1416
- Mitra S., Choudhury T. R., Ratra B., 2018b, *MNRAS*, **479**, 4566
- Mitra S., Park C.-G., Choudhury T. R., Ratra B., 2019, *MNRAS*, **487**, 5118
- Mittal S., Kulkarni G., 2021, *MNRAS*, **503**, 4264
- Mortonson M. J., Hu W., 2008, *ApJ*, **672**, 737

Nhan B. D., Bordenave D. D., Bradley R. F., Burns J. O., Tauscher K., Rapetti D., Klima P. J., 2018, arXiv e-prints, p. [arXiv:1811.04917](#)

O’Meara J. M., Prochaska J. X., Worseck G., Chen H.-W., Madau P., 2013, *ApJ*, **765**, 137

Ocvirk P., et al., 2016, *MNRAS*, **463**, 1462

Ocvirk P., Aubert D., Chardin J., Deparis N., Lewis J., 2019, *A&A*, **626**, A77

Oesch P. A., et al., 2014, *ApJ*, **786**, 108

Oesch P. A., Bouwens R. J., Illingworth G. D., Labbé I., Stefanon M., 2018, *ApJ*, **855**, 105

Omukai K., Palla F., 2001, *ApJ*, **561**, L55

Paardekooper J.-P., Khochfar S., Dalla Vecchia C., 2015, *MNRAS*, **451**, 2544

Pandey K. L., Choudhury T. R., Sethi S. K., Ferrara A., 2015, *MNRAS*, **451**, 1692

Pandolfi S., Ferrara A., Choudhury T. R., Melchiorri A., Mitra S., 2011, *Phys. Rev. D*, **84**, 123522

Park J., Mesinger A., Greig B., Gillet N., 2019, *MNRAS*, **484**, 933

Park J., Gillet N., Mesinger A., Greig B., 2020, *MNRAS*, **491**, 3891

Patra N., Subrahmanyan R., Raghunathan A., Udaya Shankar N., 2013, *Experimental Astronomy*, **36**, 319

Planck Collaboration et al., 2014, *A&A*, **571**, A15

Planck Collaboration et al., 2016, *A&A*, **594**, A13

Planck Collaboration et al., 2020, *A&A*, **641**, A6

Pospelov M., Pradler J., Ruderman J. T., Urbano A., 2018, *Phys. Rev. Lett.*, **121**, 031103

Press W. H., Schechter P., 1974, *ApJ*, **187**, 425

Prochaska J. X., O’Meara J. M., Worseck G., 2010, *ApJ*, **718**, 392

Qin Y., et al., 2017, *MNRAS*, **472**, 2009

Qin Y., Poulin V., Mesinger A., Greig B., Murray S., Park J., 2020, *MNRAS*, **491**, 1000

Reis I., Fialkov A., Barkana R., 2020, arXiv e-prints, p. [arXiv:2008.04315](#)

Ribaud J., Lehner N., Howk J. C., 2011, *ApJ*, **736**, 42

Sarmiento R., Scannapieco E., Côté B., 2019, *ApJ*, **871**, 206

Schaerer D., 2002, *A&A*, **382**, 28

Schauer A. T. P., Liu B., Bromm V., 2019, *ApJ*, **877**, L5

Schirber M., Bullock J. S., 2003, *ApJ*, **584**, 110

Schmit C. J., Pritchard J. R., 2018, *MNRAS*, **475**, 1213

Seiffert M., et al., 2011, *ApJ*, **734**, 6

Shang C., Bryan G. L., Haiman Z., 2010, *MNRAS*, **402**, 1249

Sharma P., 2018, *MNRAS*, **481**, L6

Sheth R. K., Tormen G., 1999, *MNRAS*, **308**, 119

Sheth R. K., Mo H. J., Tormen G., 2001, *MNRAS*, **323**, 1

Sims P. H., Pober J. C., 2020, *MNRAS*, **492**, 22

Singh S., Subrahmanyan R., 2019, *ApJ*, **880**, 26

Singh S., et al., 2017, *ApJ*, **845**, L12

Slatyer T. R., Wu C.-L., 2018, *Phys. Rev. D*, **98**, 023013

Sokolowski M., et al., 2015, *Publ. Astron. Soc. Australia*, **32**, e004

Songaila A., Cowie L. L., 2010, *ApJ*, **721**, 1448

Sunyaev R. A., Zeldovich Y. B., 1980, *MNRAS*, **190**, 413

Telfer R. C., Zheng W., Kriss G. A., Davidsen A. F., 2002, *ApJ*, **565**, 773

Valiante R., Schneider R., Volonteri M., Omukai K., 2016, *MNRAS*, **457**, 3356

Visbal E., Haiman Z., Terrazas B., Bryan G. L., Barkana R., 2014, *MNRAS*, **445**, 107

Vishniac E. T., 1987, *ApJ*, **322**, 597

Voytek T. C., Natarajan A., Jáuregui García J. M., Peterson J. B., López-Cruz O., 2014, *ApJ*, **782**, L9

Wise J. H., Demchenko V. G., Halicek M. T., Norman M. L., Turk M. J., Abel T., Smith B. D., 2014, *MNRAS*, **442**, 2560

Wolcott-Green J., Haiman Z., Bryan G. L., 2011, *MNRAS*, **418**, 838

Wu X., McQuinn M., Kannan R., D’Aloisio A., Bird S., Marinacci F., Davé R., Hernquist L., 2019, *MNRAS*, **490**, 3177

Yajima H., Choi J.-H., Nagamine K., 2012, *MNRAS*, **427**, 2889

Yung L. Y. A., Somerville R. S., Popping G., Finkelstein S. L., Ferguson H. C., Davé R., 2019, *MNRAS*, **490**, 2855

## APPENDIX A: COMPARISON WITH THE “TRADITIONAL” CONSTRAINTS FROM CMB

In this appendix, we show some comparisons of our model with the traditional methods of constraining parameters using the CMB data. For the **traditional-CMB** analysis, we assume the reionization history to have a tanh form (Planck Collaboration et al. 2020). The results are then compared with the **only-CMB** analysis of Section 3.1 where we use only the CMB data to constrain the parameters using the CF reionization model. The posterior distributions of the model parameters for the two cases are shown in Figure A1.

As is evident from this figure, the constraints on cosmological parameters are not much different between the two analyses, except for  $\sigma_8$  and  $\tau$ . The mean value of  $\tau$  comes out to be 0.058 for the **only-CMB** analysis which is somewhat higher than that obtained from the **traditional-CMB** analysis ( $\tau = 0.052$ ). Also, the 95% upper limit of  $\tau$  is 0.08 for the **only-CMB** is higher than that obtained from the **traditional-CMB** analysis (0.07). To investigate this in more detail, we have plotted reionization histories coming from the **only-CMB** analysis with the **traditional-CMB** in Figure A2. The light-green shaded region shows the evolution of the volume fraction of ionized Hydrogen ( $Q_{\text{HII}}$ ) corresponding to 1000 random samples obtained from the MCMC chains of the **only-CMB** analysis. The green curve corresponds to the best-fit values of the free parameters of this analysis. The orange curve corresponds to best-fit values obtained from the **traditional-CMB** analysis. It is very evident that the allowed CF reionization histories are very different from that of the tanh model. In the CF models, the reionization process starts early (around  $z = 10$ ) but extends to much later redshift showing a much slower evolution with redshift compared to the tanh reionization. This extended tail in CF reionization explains the higher value of  $\tau$  compared to the traditional Planck estimate. Because  $\sigma_8$  and  $\tau$  are strongly correlated, higher values of  $\tau$  will induce higher values for  $\sigma_8$  as well.

The log-likelihood ( $\mathcal{L}_{\text{pl}}$ ) of the best-fit model for the **only-CMB** analysis turns out to be  $\sim 694$  which is marginally less than that coming from **traditional-CMB** analysis ( $\mathcal{L}_{\text{pl}} \sim 696$ ), suggesting that the CF reionization model is an equally good (if not better) match to the data as compared to the traditional tanh model.

This paper has been typeset from a  $\text{\LaTeX}$  file prepared by the author.

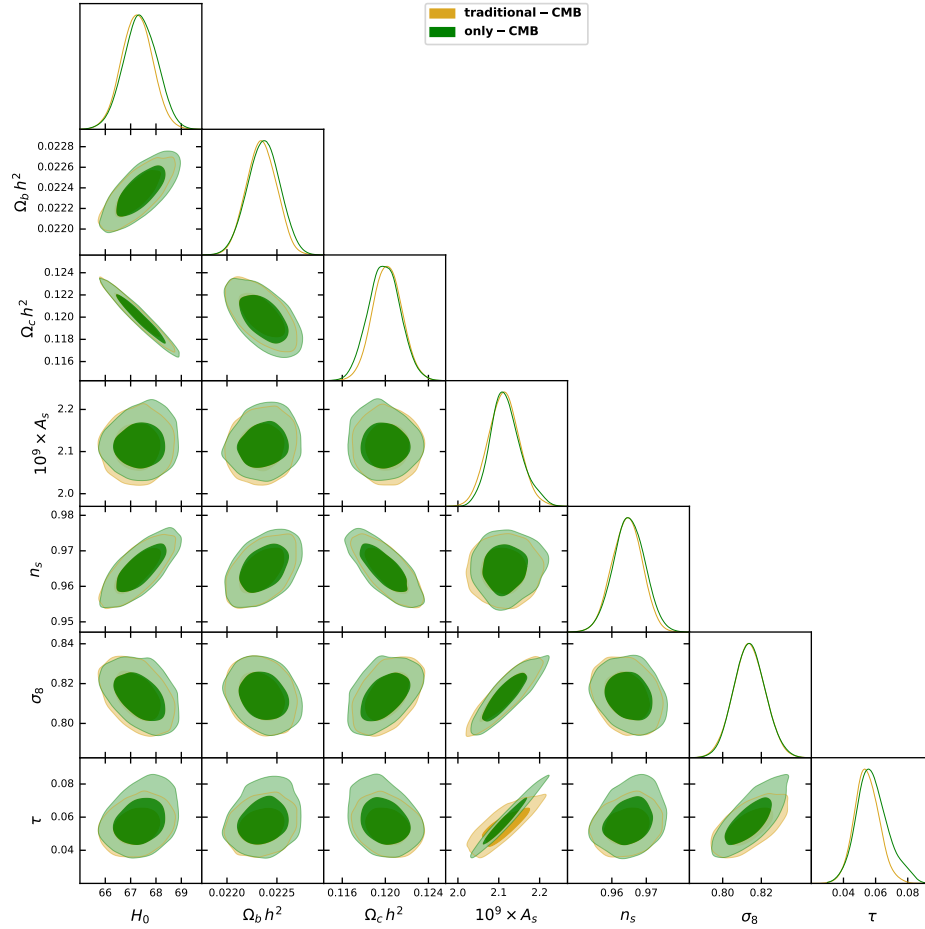


**Figure A1.** The marginalized posterior distributions of cosmological parameters obtained from **only-CMB** (green) and **traditional-CMB** (orange) analyses. We show the 68% and 95% confidence contours in the two-dimensional plots. Note that  $\sigma_8$  and  $\tau$  are derived parameters while the others are free parameters in our model.

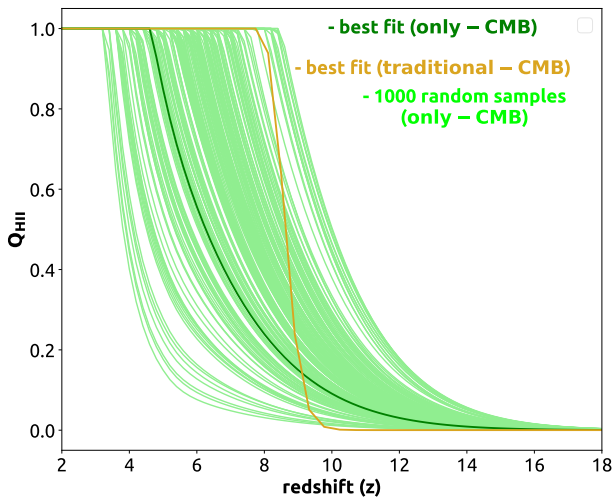


**Figure A2.** redshift evolution of the volume filling factor of HII region ( $Q_{\text{HII}}$ )